Figure 4 (See legend on next page.)

(See figure on previous page.)
Figure 4 Paraspeckles appear predominantly in spinal motor neurons in ALS. A. RNA-FISH using DIG-labeled NEAT1_2 probe indicates that NEAT1_2 lncRNA often appears in the nuclei of human motor neurons in sporadic ALS cases. Right panel shows the profile image of fluorescence intensity of NEAT1_2 lncRNA and TDP-43 along the arrow in the nucleus (ZEN software, Carl Zeiss). Most NEAT1_2 signals overlapped with parts of aggregated TDP-43 in the nucleus (arrowheads). Dotted lines represent the outline of the nucleus. **B**. No NEAT1_2 expression is detected in most motor neurons in control cases. Dotted lines represent the outline of the nucleus. **C**. A 40-fold magnified view of a spinal motor neuron in an ALS case is shown with DAB-hematoxylin counterstain using anti-PSP1 antibody. The arrowhead indicates the nucleolus. Arrows indicate PSP1 aggregates in the nucleus. **D, E**. RNA-FISH using DIG- or FITC-labeled NEAT1_2 probe in the nuclei of ALS motor neurons. PSF ((D), ALS-Pt C), PSP1 (upper in (E), ALS-Pt D) and p54^{nrb} (lower in (E), ALS-Pt B) overlap with NEAT1_2 foci. Observation at 647 nm wavelength was performed to rule out autofluorescent signals. Right panels display images on orthogonal sections (ZEN software). Asterisks indicate lipofuscin in the cytoplasm. Dotted line: outline of the nucleus. Scale bars, 10 μm.

At Stage 0, TDP-43 is normally distributed within the nucleus. Since TDP-43 is seen in the cytoplasm or the nucleus of the motor neuron degrades, stage I, II and III indicate pathological stages in ALS. The nucleus degrades but is still recognized at stage I. In stage II, the nuclear TDP-43 was not recognized any more, however, the plasma membrane seems still retained. Stage III is the final stage, where the plasma membrane disappeared and TDP-43 skein-like inclusions are left behind. ALS cases demonstrated motor neurons at all pathological stages, in contrast to control cases in which all motor neurons were limited to stage 0 (Figure 5B). In overall counting of the motor neurons in the ventral horn, there was no significant difference in the NEAT1_2 lncRNA appearance rate between in ALS and control cases (Additional file 5: Figure S5). Only at stage 0, however, the occurrence of NEAT1_2 expression in motor neurons was significantly increased in ALS cases compared to that in control cases (85.6 ± 11.0% and 35.1 ± 22.6%, respectively; Figure 5C). The positive rate of NEAT1_2 foci in motor neurons was higher at the early stage of ALS than at the advanced stage (Figure 5D). This finding suggests that NEAT1_2 lncRNA appeared preferentially in spinal motor neurons at the earliest point of ALS.

Characterization of nuclear paraspeckles by electron microscopy

The nuclear distribution pattern of NEAT1_2 lncRNA in the human nervous system has not been previously reported, and its function remains largely unknown. To observe NEAT1_2 localization in human spinal motor neurons in detail, electron microscopic analysis combined with *in situ* hybridization (EM-ISH) was performed. In the spinal cords of human ALS cases, NEAT1_2 lncRNA was localized to IGAZ in a halo-like fashion, suggesting that NEAT1_2 lncRNA formed the characteristic structure of paraspeckles in the nuclei of spinal motor neurons in ALS cases (Figure 6B-a and -b, and Additional file 6: Figure S6C), consistent with previous articles [17,28,30]. By contrast, NEAT1_2-labeled gold particles around IGAZ were rare in control cases

(Figure 6B-c and -d). The IGAZ has been considered to be identical to a paraspeckle [17,28-30], indicating that the formation of IGAZ depends on NEAT1_2 lncRNA. IGAZ-like zone without NEAT1_2 granules in Figure 6B-d suggests that a human motor neuron has a moderately electron-dense intranuclear structure besides paraspeckles. Alternatively, independent of NEAT1_2 lncRNA, IGAZ may exist in the nucleus as a scaffold prior to the recruitment of NEAT1_2 lncRNA to form a complete paraspeckle. NEAT1_1/1_2 probe, detecting both NEAT1_1 ncRNA and NEAT1_2 lncRNA (Additional file 1: Figure S1D, upper), was observed in the nuclei of spinal motor neurons in control cases as frequently as those in ALS cases (Additional file 6: Figure S6A-a, -b, -c and -d). Notably, halo-shaped aggregation patterns formed by NEAT1_1/1_2 ncRNAs were found throughout nuclei in ALS spinal motor neurons (Additional file 6: Figure S6A-b) but were observed rarely in control cases (Additional file 6: Figure S6A-c and -d). Even when diluted NEAT1_1/1_2 probe is used, both central (Additional file 6: Figure S6B-a) and halo-like (Additional file 6: Figure S6B-b) patterns of aggregation were observed in a HeLa cell. This suggests that NEAT1_1 ncRNA may show the central accumulation pattern independently of the IGAZ margin; however, it could demonstrate the halo-shaped pattern depending on NEAT1_2 lncRNA. Taken these findings together, NEAT1_2 lncRNA forms paraspeckles specifically around IGAZ in the nuclei of motor neurons in ALS cases, which may affect the distribution of NEAT1_1 ncRNA.

Discussion

In this study, we demonstrated that a lncRNA with GC-rich sequence, NEAT1_2, is predominantly expressed in spinal motor neurons in an early phase of the ALS pathological process. To our knowledge, this report is the first to indicate a direct association of paraspeckle formation with a human neurodegenerative disease.

The involvement of abnormalities in functional RNAs has been reported in the development of various neurodegenerative disorders. For example, (CAG)n triplet repeats encoding polyglutamine induce spinocerebellar ataxia type 2; however, when glutamine-coding sequences
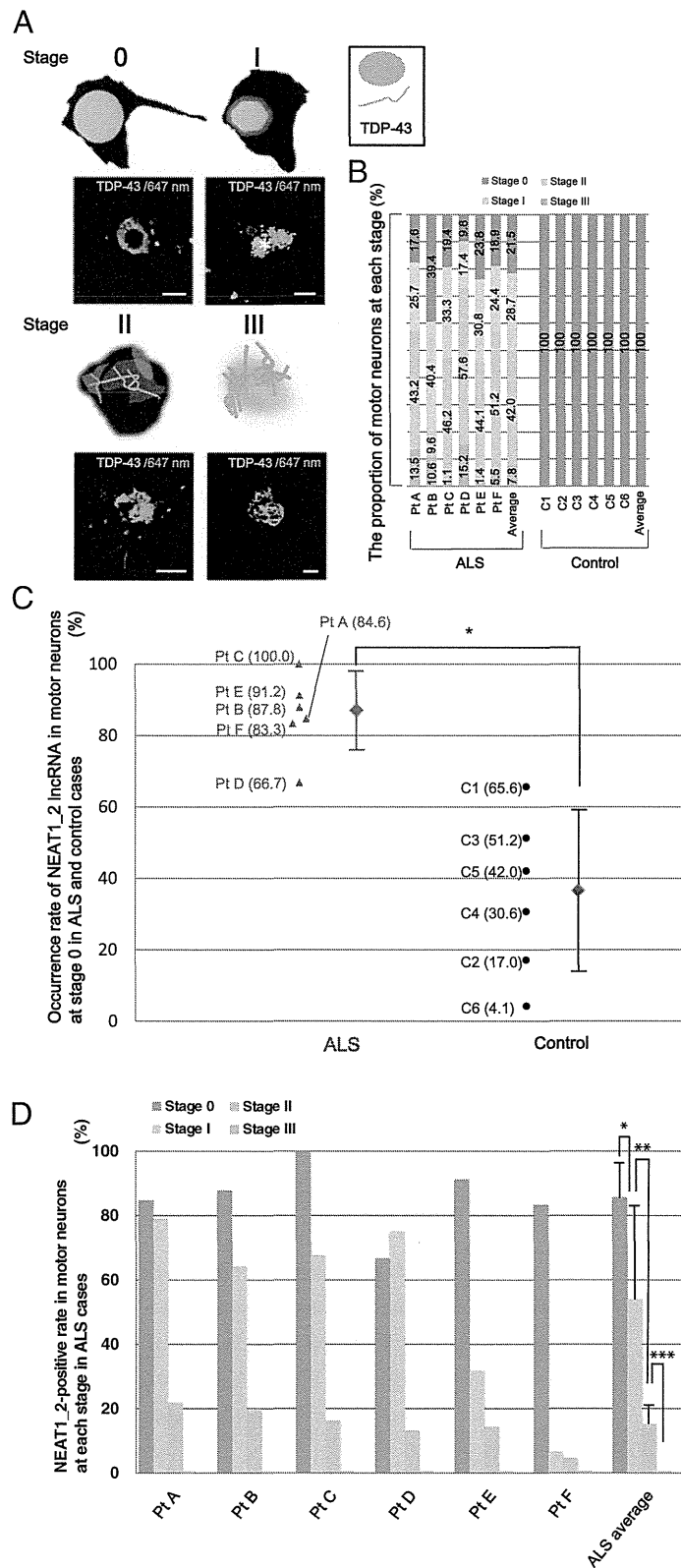
Figure 5 (See legend on next page.)

(See figure on previous page.)
Figure 5 Paraspeckle formation is frequently observed in an early phase of ALS. A. A scheme of TDP-43 aggregation patterns in ALS is presented. Observations detected at 647 nm are added to distinguish the TDP-43-positive signals from autofluorescence produced by lipofuscin granules in the cytoplasm (shown as an asterisk). Scale bars, 10 μm. **B**. Stages of motor neurons in sporadic ALS and control cases are shown according to the definitions in Table 2. The number on the bar graph represents the proportion of motor neurons at each stage in a case. **C**. NEAT1_2-positive rates in the spinal motor neurons at stage 0 are indicated (ALS vs. control). Each triangle or circle represents an individual ALS (Pt) or control (C) patient, respectively. The actual value of percentage in each case is shown in parenthesis. Bars represent the mean ± s.d.; that is, 85.6 ± 11.0% in ALS cases and 35.1 ± 22.6% in control cases (n = 6 per group). *$P<0.001$. **D**. NEAT1_2-positive rates in spinal motor neurons at each stage are plotted. Mean ± s.d. were 54.0 ± 28.6% at stage I, 15.1 ± 6.1% at stage II, and 0.0 ± 0.0% at stage III (n = 6 per group). *$P<0.05$, **$P<0.01$, ***$P<0.001$.

(CAA)s are inserted into the CAG repeats, this genotype becomes a risk factor for ALS [37]. Moreover, (GGGGCC) n hexanucleotide repeat expansion in ALS has been described in the intron of the C9ORF72 gene recently. Any ALS cases in the present study did not have (GGGGCC) hexanucleotide repeat expansion, but previous report showed that RNA consisting of GGGGCC-expanded repeats formed characteristic foci in the nuclei of human spinal motor neurons [3]. These findings suggest that alteration in RNA metabolism may be important for the ALS pathomechanism in specific nuclear foci including RNAs with the GC-rich sequence.

Full-length and 35-kDa TDP-43 were retained in NEAT1_2 foci (Figure 1A, B, and Additional file 1: Figure S1A), suggesting that the appearance of NEAT1_2 lncRNA may change functions of these TDP-43 proteins to process RNAs and to form stress granules. By contrast, NEAT1_2 foci did not retain the 26-kDa fragment of TDP-43 (Figure 1A, B). Even when NEAT1_2 lncRNA appears in the nucleus, insoluble 26-kDa TDP-43 with phosphorylation is mislocalized to the cytoplasm, consistent with previous pathological findings [12].

The direct binding of TDP-43 or FUS/TLS to NEAT1_2 lncRNA was verified in Figure 2C. In a recent article, iCLIP data targeting TDP-43 suggested that NEAT1_2 lncRNA was one of the target RNAs bound predominantly by TDP-43 in human brain tissue with TDP-43 proteinop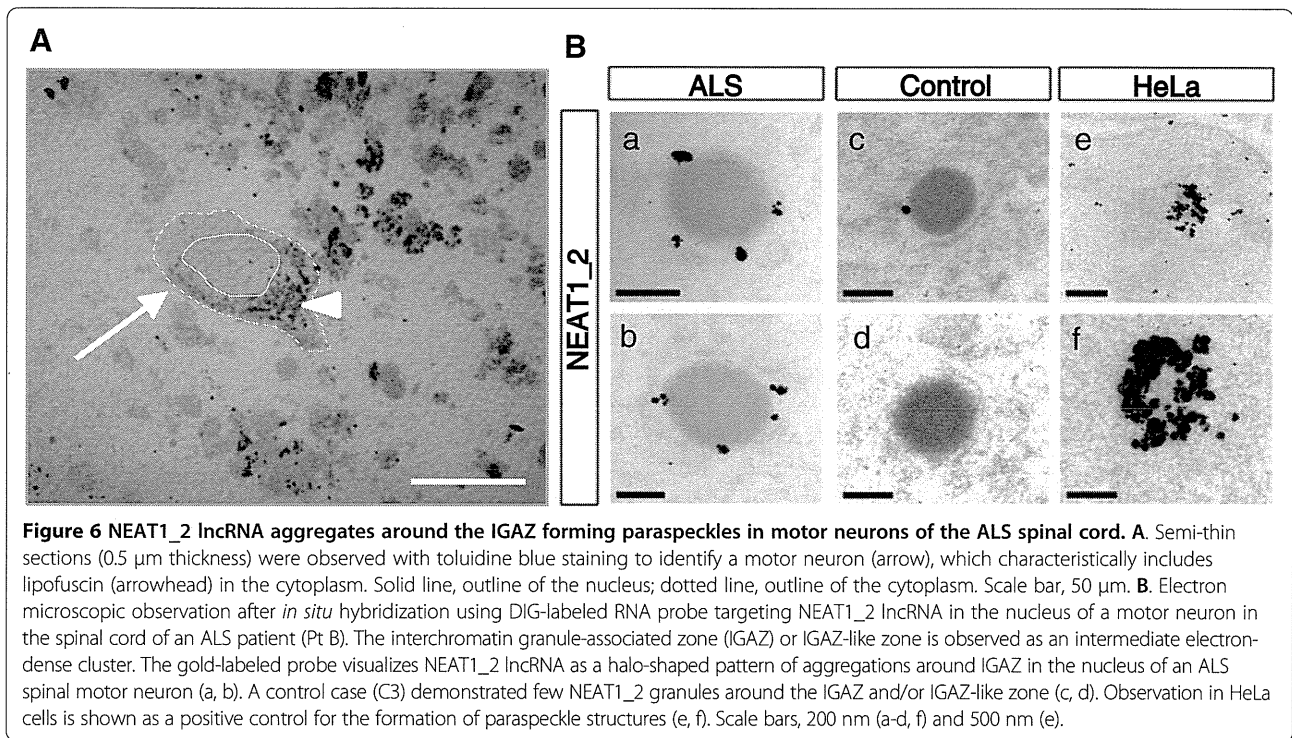athy and cultured cells [23]. According to this report, 5% of TDP-43 iCLIPed cDNA was mapped to lncRNA regions, and TDP-43 demonstrated high binding affinities to UG-repeat clusters in positions 6,662–6,728 and 21,464–21,544 of NEAT1_2 lncRNA (Additional file 7: Figure S7). Additionally, another recent report presented proteomic evidence for TDP-43 co-aggregation with several paraspeckle proteins, suggesting that paraspeckle formation may have a strong influence on the localization and function of TDP-43 in the nucleus [38].

Similarly, previous reports indicated that NEAT1_2 lncRNA is one of the RNAs directly bound by FUS/TLS. Wang et al. demonstrated that FUS/TLS preferentially interacts with GGUG RNA oligonucleotides [24]. Another recent report using iCLIP methods in mouse brain also revealed that the GGU motif increases the affinity of FUS/TLS for RNA [25]. Using mouse and human brain, the latest CLIP-seq data showed enrichment of the GUGGU motif in FUS/TLS clusters [26]. These reports suggest that UG-rich sequences are the preferred binding sites of both TDP-43 and FUS/TLS; however, Rogelj et al. did not mention any overlap between the sequence specificity of TDP-43 and FUS/TLS [25]. By contrast, PAR-CLIP procedure revealed that the FUS/TLS-binding sites frequently involve the *SON* cluster or AU-rich stem-loops, unlike the previous reports described above [27]. This procedure revealed NEAT1 ncRNA to be a target of both WT and mutant FUS/TLS. Interestingly, one more binding site in NEAT1

Table 2 Pathological staging of motor neurons in ALS according to TDP-43 distribution

Stage 0	TDP-43 is normally distributed within the well-marginated nucleus.			
Stage I	The nucleus degradated, and TDP-43 was also seen in the cytoplasm.			
Stage II	The nuclear TDP-43 was so cleared that it was not recognized.The plasma membrane was still retained.			
Stage III	The plasma membrane disappeared.			

	TDP-43 distribution		nuclear membrane	plasma membrane
	in the nucleus	in the cytoplasm		
Stage 0	+	-	+	+
Stage I	+	+	±	+
Stage II	ND	+	-	+
Stage III	ND	ND	-	-

ND, not determined.

Figure 6 NEAT1_2 lncRNA aggregates around the IGAZ forming paraspeckles in motor neurons of the ALS spinal cord. A. Semi-thin sections (0.5 μm thickness) were observed with toluidine blue staining to identify a motor neuron (arrow), which characteristically includes lipofuscin (arrowhead) in the cytoplasm. Solid line, outline of the nucleus; dotted line, outline of the cytoplasm. Scale bar, 50 μm. **B**. Electron microscopic observation after *in situ* hybridization using DIG-labeled RNA probe targeting NEAT1_2 lncRNA in the nucleus of a motor neuron in the spinal cord of an ALS patient (Pt B). The interchromatin granule-associated zone (IGAZ) or IGAZ-like zone is observed as an intermediate electron-dense cluster. The gold-labeled probe visualizes NEAT1_2 lncRNA as a halo-shaped pattern of aggregations around IGAZ in the nucleus of an ALS spinal motor neuron (a, b). A control case (C3) demonstrated few NEAT1_2 granules around the IGAZ and/or IGAZ-like zone (c, d). Observation in HeLa cells is shown as a positive control for the formation of paraspeckle structures (e, f). Scale bars, 200 nm (a-d, f) and 500 nm (e).

ncRNA was identified using mutant FUS/TLS than using WT FUS/TLS, suggesting the possibility that the affinity or binding pattern of mutant FUS/TLS may differ from that of WT FUS/TLS [27]. Here, we found that the NEAT1_2 sequence possessed at least three similar stem-loops to the *SON* cluster that was proposed as a FUS/TLS-binding site (Additional file 7: Figure S7). In particular, the most upstream cluster, which starts from the nucleotide at position 3,440, is highly AU-rich in content, suggesting that FUS/TLS binds most preferably to this site of NEAT1_2 lncRNA.

Importantly, the frequency of paraspeckle formation increased significantly during the early phase of ALS pathological course (Figure 5C, D). The possibility that aging simply induced an increase in the level of NEAT1_2 lncRNA was eliminated based on two observations. First, NEAT1_2 lncRNA did not appear in the spinal motor neurons of 2-y-old control mice (Figure 3B), and second, human control cases in this study were older than ALS cases by an average of 10 y (Table 1). The ventral spinal motor neurons include α- and γ-motor neurons besides interneurons. Here, we counted all spinal motor neurons on the slides. In the normal condition, α-motor neurons can be distinguished definitely from γ-motor neurons and interneurons by the size; that is, α- for more than 35 μm and γ- and interneurons for less than 35 μm. In this study, however, the α-motor neurons had degenerated to get smaller, looking like γ-motor neurons or interneurons. To the best of our

knowledge, any reliable molecular marker has never been verified to stain α-motor neurons specifically in the human tissue. Therefore, we could not investigate the difference of NEAT1_2 lncRNA occurrence according to the type of neurons in the spinal cord. Developing the specific human marker of the α-motor neuron, further investigations are required to determine this point.

This would be also among the first reports to show EM-ISH images focusing on the nuclei of human motor neurons. We confirmed that the NEAT1_2 foci in motor neurons demonstrated characteristics of paraspeckle formation, in which the NEAT1_2 probe revealed a halo-like appearance around IGAZs (Figure 4C–E and Figure 6B). By contrast, the NEAT1_1/1_2 probe often demonstrated a central accumulation pattern, but occasionally formed the halo-like pattern in the presence of NEAT1_2 lncRNA (Additional file 6: Figure S6A, B). These results indicate that NEAT1_2 lncRNA may influence NEAT1_1 ncRNA localization and possibly function.
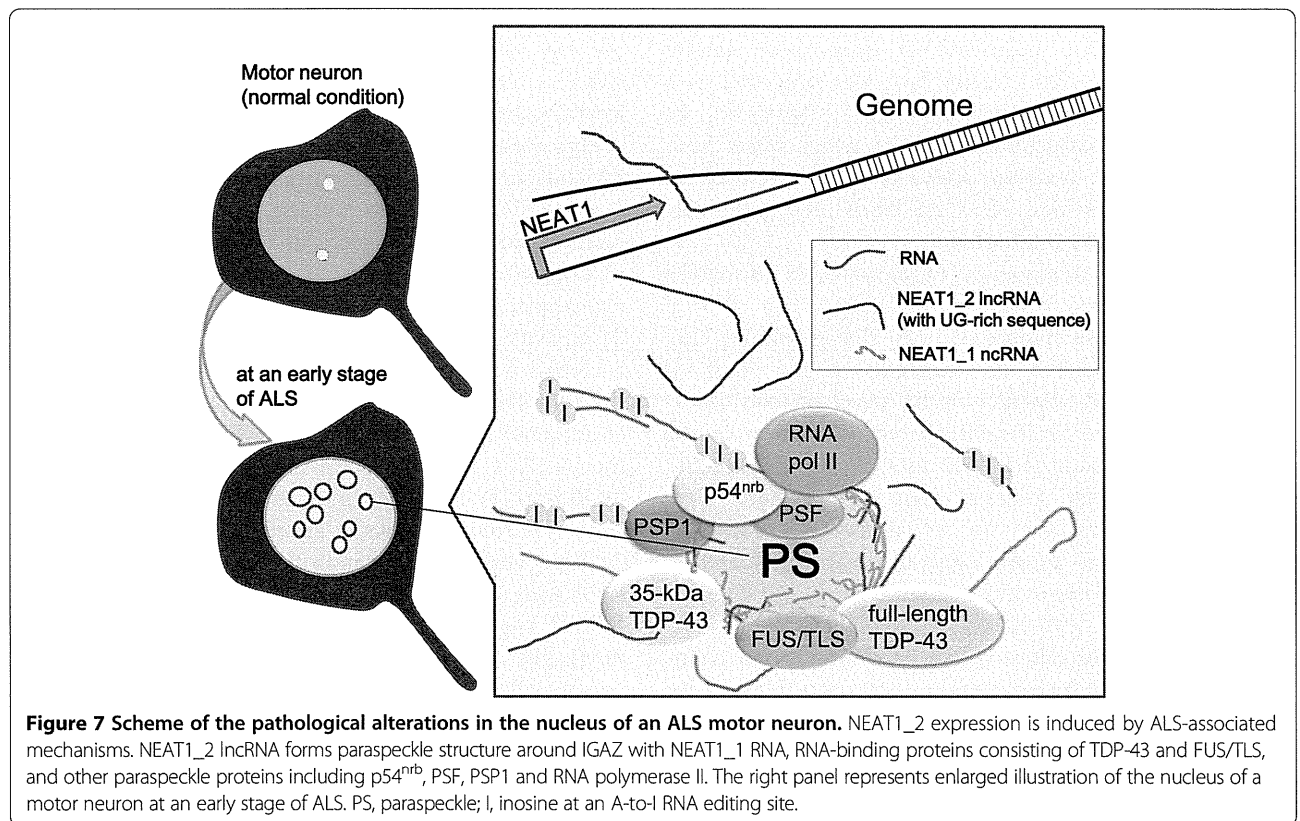
As reported previously, *Lin28* mRNA transcript and cationic amino acid transporter 2 transcribed nuclear RNA with hyper-edited sites are retained in paraspeckles [15,16], suggesting that RNA editing alterations may dynamically change cell fate by retaining RNA in paraspeckles. Insufficient GluA2 mRNA (Q/R-)editing efficiencies in motor neurons were identified specifically in sporadic ALS cases [14]. Translation of a small amount of the edited GluA2 mRNA in ALS could potentially be suppressed through paraspeckle formation,

while unedited GluA2 mRNA is perhaps predominantly released from nuclear paraspeckles into the cytoplasm, causing toxicity to motor neurons.

Both TDP-43 and FUS/TLS are paraspeckle proteins, which are required for normal paraspeckle formation through the direct interactions with NEAT1_2 lncRNA. According to the previous report using cultured cells, the number and size of paraspeckles were decreased significantly by TDP-43 RNAi, and paraspeckle formation was completely disrupted under the FUS/TLS knockdown [33]. FUS/TLS also associates with RNA polymerase II, which is another paraspeckle protein [39,40]. RNA polymerase II is not only responsible for polyadenylation, but also for determination of the 3'-end-point in pre-mRNA processing in cooperation with other paraspeckle proteins, PSF and $p54^{nrb}$ [41,42]. Paraspeckle proteins could induce processing of target RNAs bound to FUS/TLS or TDP-43 in ALS spinal motor neurons [43]. The components of the paraspeckle, including RNA polymerase II, PSF and $p54^{nrb}$, may produce RNAs with their 3'UTRs truncated, which could be resistant to microRNAs. Screening of the target RNAs assembled in the paraspeckles will be highly informative. In particular, identification of 3'-end sites or alternative splicing patterns of target RNAs may be key for future investigations.

The summarized scheme at an early phase of ALS is shown in Figure 7. Certain stresses may cause NEAT1_2 lncRNA-induced paraspeckle formation in the nucleus, however, it still remains unknown what mechanism is involved in the upregulation of NEAT1_2 lncRNA during early phase of ALS.

The recent reports have described lncRNA could be subject to epigenetic regulation, especially histone methylation, depending on cell types; thus, investigation of the distribution and levels of H3K4 and H3K27 methylation is required to understand regulation mechanism of NEAT1_2 lncRNA in the future [44]. The paraspeckle retains functional RNA-binding proteins including TDP-43, FUS/TLS, and the other paraspeckle proteins, culminating in an ectopic structure that may serve as a platform for RNA metabolism associated with ALS. Hyper-edited RNAs and/or RNAs preferably bound to paraspeckle component proteins may be captured in paraspeckles and processed aberrantly prior to export to the cytoplasm. There is another possibility that paraspeckles with the NEAT1_2 lncRNAs appear under certain stressful condition during early phase of ALS and alleviate the toxicity by regulating the specific RNA splicing events and/or the 3'UTR determinations. As the pathological stage progresses, neuronal degeneration might occur with the decrease of paraspeckles.

Figure 7 Scheme of the pathological alterations in the nucleus of an ALS motor neuron. NEAT1_2 expression is induced by ALS-associated mechanisms. NEAT1_2 lncRNA forms paraspeckle structure around IGAZ with NEAT1_1 RNA, RNA-binding proteins consisting of TDP-43 and FUS/TLS, and other paraspeckle proteins including $p54^{nrb}$, PSF, PSP1 and RNA polymerase II. The right panel represents enlarged illustration of the nucleus of a motor neuron at an early stage of ALS. PS, paraspeckle; I, inosine at an A-to-I RNA editing site.

Screening of the target RNAs assembled in the para-speckles with RNA-binding proteins will also be highly informative. In particular, identification of 3'-end position or alternative splicing patterns of target RNAs and regulation in microRNA biogenesis may be key for future investigations as described above. Success in this screening largely depends on technological innovation in the field of CLIP and RNA sequencing [27,45,46].

For the next step, another investigation into changes of phenotype after crossing ALS model mice with NEAT1_2 knockout mice is required to verify, at least in part, whether the increase in NEAT1_2 lncRNA has a protective or damaging role in the ALS pathological pathway. Additionally, NEAT1_2 knock-in mice and human induced pluripotent stem cells-derived motor neurons under exogenous NEAT1_2 expression should be characterized.

In conclusion, this study identified the 'paraspeckle' formation containing a nuclear lncRNA, NEAT1_2, in the early phase of ALS, shedding light on novel therapeutics for motor neuron degeneration.

Materials and methods
Cell culture and reagents
HeLa human carcinoma cells were maintained in Dulbecco's modified Eagle's medium (Gibco, Grand Island, NY) supplemented with 10% fetal bovine serum as described previously [8,47]. Transfection was performed using GeneJuice Transfection Reagent (Novagen, Madison, WI) according to the manufacturer's instructions. To transfect HeLa cells, cells were grown to 60–80% confluence on 0.001% poly-L-lysine (PLL)-coated coverslips or 8-chamber slides (Chamber slide II, Iwaki Glass, Tokyo, Japan). Forty-eight hours after transfection, cells were fixed in 4% paraformaldehyde (PFA) overnight at 4°C for *in situ* hybridization or for 10 min at room temperature for immunofluorescence staining. Cells were washed with phosphate-buffered saline (PBS), and total RNA was extracted using TRIzol reagent (Invitrogen, Carlsbad, CA) for quantitative RT-PCR.

Human tissue frozen samples and animal tissue samples
Human spinal cords were stored at -80°C immediately after removal from the body. Informed consent was given by the legal guardians of the patients and all experimental procedures in this study were carried out in accordance with the Declaration of Helsinki principles and with the approval of the Ethics Committees of School of Medicine, Keio University (no. 20100268), Tokyo Metropolitan Geriatric Hospital (no. 73), RIKEN Advanced Science Institute (no. 23-3), and Institute of Brain and Blood Vessels, Mihara Memorial Hospital (no. 049-01). To quantify RNA expression levels, 8-week-old C57BL/6 mice were anesthetized with pentobarbital and

perfused with PBS, and then each tissue was eluted in TRIzol followed by RNA extraction and quantitative RT-PCR. For staining, perfusion was performed with 4% PFA in PBS. All animal experiments were conducted in accordance with an animal protocol approved by the Laboratory Animal Care and Use Committee of Keio University. Tissues were then resected for cryoprotection with 20% sucrose in PBS and embedded in Tissue-Tek (Sakura Finetek, Torrance, CA). Sections of human or mouse dissected tissues (14 μm thick) on PLL-coated glass slides (Matsunami Glass, Osaka, Japan) were dried and refixed in 4% PFA overnight at 4°C, followed by immunofluorescence staining, *in situ* hybridization, or immunohistochemistry as described below.

Antibodies
Among primary antibodies, mouse monoclonal anti-V5 (1:500, R960-25) was purchased from Invitrogen. Rabbit polyclonal anti-V5 (1:500, A190-120A) and rabbit polyclonal anti-FUS/TLS (1:250, A300-302A) were from Bethyl Labs (Montgomery, TX). Rabbit polyclonal anti-TDP-43 (1:250, 10782-2-AP) was from Proteintech (Chicago, IL). These polyclonal antibodies directed against FUS/TLS and TDP-43 were used for immuno-chemistry and immunoprecipitation. Mouse monoclonal antibodies, anti-TDP-43 (1:1,000, H00023435-M01) from Abnova (Walnut, CA) and anti-FUS/TLS (1:1,000, 4H11, sc-47711) from Santa Cruz Biotechnology (Santa Cruz, CA), were used for immunoblotting. Rabbit polyclonal anti-fluorescein isothiocyanate (FITC) (1:500, ab19491), mouse monoclonal anti-digoxigenin (DIG) IgG1 (1:500, H8, ab420), and mouse monoclonal anti-coilin IgG2b (1:500, IH10, ab87913) were from Abcam (Cambridge, MA). Mouse monoclonal anti-β-actin (1:10,000, AC-15, A1978) and anti-PSF (1:200, B92, P2860) antibodies were from Sigma (St. Louis, MO). Mouse monoclonal anti-p54^{nrb} (1:200, 3/p54nrb, 611279) was from BD Transduction Laboratories (San Diego, CA). Rabbit polyclonal anti-PSP1 (1:500) was generated by T. H. The secondary antibodies used for immunofluorescence, Alexa Fluor 488 goat anti-rabbit IgG (A-11034), Alexa Fluor 488 goat anti-mouse IgG1 (A-21121), Alexa Fluor 488 goat anti-mouse IgG2b (A-21141), Alexa Fluor 555 goat anti-rabbit IgG (A-21429), Alexa Fluor 555 goat anti-mouse IgG (A-21424), Alexa Fluor 555 goat anti-mouse IgG1 (A-21127), and Alexa Fluor 647 goat anti-mouse IgG2b (A-21242), were purchased from Life Technologies (Carlsbad, CA).

Vectors
Plasmids containing the V5-tagged series of TDP-43 and FUS/TLS were kindly provided by Dr. Daisuke Ito (Keio University) [8,9].

RNA-FISH

Fixed cells or tissues on PLL-coated glass slides were treated with 0.2 N HCl for 20 min, followed by 3 μg/ml proteinase K (PCR grade; Roche, Indianapolis, IN) at 37°C for 3 min (in the case of cell samples) or 7 min (in the case of tissue samples). After acetylation in a solution consisting of 1.5% triethanolamine, 0.25% acetic anhydride, and 0.25% HCl, the hybridization reaction was carried out with DIG- or FITC-labeled probes (1 μg/ml) for 16 h at 55°C in hybridization buffer (50% formamide, 2× SSC, 1× Denhardt's solution, 5% dextran sulfate, 10 mM ethylenediaminetetraacetic acid (EDTA), and 0.01% Tween 20). Samples were washed twice at 55°C for 30 min with a solution consisting of 50% formamide, 2× SSC, and 0.01% Tween 20, and then 10 μg/ml RNase A was added at 37°C for 1 h in buffer (0.5 M NaCl, 10 mM Tris (pH 8.0), 1 mM EDTA, and 0.01% Tween 20). They were washed in 2× SSC wash buffer with 0.01% Tween 20 at 55°C for 30 min, followed by washing in 0.2× SSC wash buffer with 0.01% Tween 20 at 55°C for 30 min. After additional washing in Tris-buffered saline (TBS, pH 7.6) and blocking in a buffer consisting of blocking reagent (Roche 11096176001), 0.1 M maleate, 0.15 M NaCl, and 0.01% Tween 20 in TBS, DIG- or FITC-labeled probes were detected by standard immunohisto-/immunocytochemical procedures using antibodies against DIG, FITC, and other proteins.

In preparation for DIG- or FITC-labeled RNA probes, cDNA fragments were amplified using M13 forward (FW) and reverse (RV) primers with the AV089414 EST clone as a template for the mouse NEAT1_1/1_2 probe. cDNA fragments were subcloned into pCRII (Invitrogen) for the mouse NEAT1_2 probe after amplification using mNEAT1_2 FW/RV primers with the BAC clone RP23-209P9 as a template [36]. For the human NEAT1_1/1_2 probe and NEAT1_2 probe, cDNA fragments were obtained using hNEAT1 FW/RV primers and hNEAT1_2 FW/RV primers, respectively, using a cDNA library derived from HeLa cells as a template and were subcloned into pCRII-TOPO (Invitrogen) and pGEM-T Easy vectors (Promega, Madison, WI). Each primer is shown in Additional file 8: Table S1. Both antisense and negative control sense RNA probes were prepared using a DIG/FITC RNA labeling mix (1277073/1685619, Roche), RNasin Plus RNase Inhibitor (N2611, Promega), and T3, T7 or SP6 RNA polymerase (P2083/ P2075/P1085, respectively, Promega) according to the manufacturer's instructions. The usability of each probe was finally characterized by Northern blot.

CLIP assay

CLIP assay was performed as described previously [48,49]. Briefly, HeLa cells were UV cross-linked at 254 nm (UV-B) with 600 J/cm^2 in a UV Stratalinker 1800 crosslinker (Stratagene, La Jolla, CA); lysed in wash buffer containing 1× PBS, 0.1% sodium dodecyl sulfate (SDS), 0.5% deoxycholate, and 0.5% NP-40; supplemented with 0.015 U/μl RNasein Plus (N261, Promega) and RQ RNase-Free DNase (M610A, Promega); and immunoprecipitated for 2 h at 4°C with 5 μg polyclonal anti-TDP-43, anti-FUS/TLS, and rabbit IgG control (AB-105-C, R&D Systems, Minneapolis, MN) antibodies bound in advance to Dynabeads Protein G (100.04 D, Invitrogen). Immunoprecipitated materials were washed as follows: twice with wash buffer described above for 5 min; twice with 5× PBS, 0.1% SDS, 0.5% deoxycholate, and 0.5% NP-40 for 5 min (using high-salt wash buffer to completely remove indirect protein-RNA interactions); and twice with 50 mM Tris-HCl (pH 7.4), 10 mM MgCl$_2$, and 0.5% NP-40 for 5 min. The immunoprecipitated protein-bead complexes were removed from RNA by proteinase K (13731196, Roche) digestion. RNA was then isolated by phenol/chloroform extraction and treated again with DNase I before the RT reaction was performed as described below. Bound RNAs were evaluated by PCR assay using the qhNEAT1_2 FW/RV primers listed in Additional file 8: Table S1. The PCR reaction was performed in a 50 μl reaction mixture containing 0.2 μM of each primer, 0.25 mM dNTP mix (Takara, Otsu, Japan), 5 μl 10× PCR buffer, and 1 μl Advantage 2 Polymerase mix (639201, Clontech, Mountain View, CA). PCR amplification began with a denaturation step at 95°C for 1 min, followed by 25, 33, or 40 cycles of denaturation at 95°C for 10 s, annealing at 64°C for 30 s, and extension at 68°C for 30 s.

Immunoblotting

Cells and UV cross-linked immunoprecipitates after stringent washes with the high-salt wash buffer were lysed in cold lysis buffer (50mM Tris–HCl, pH 7.4, 150 mM NaCl, 0.5% Nonidet P-40, 0.5% sodium deoxycholate, 0.25% SDS, 5mM EDTA and Complete, EDTA-free Protease Inhibitor Cocktail Tablets (1873580, Roche)). The input cell lysate was briefly sonicated and lysed samples were separated via reducing SDS-PAGE on a 4–20% Tris-glycine gradient gel (Invitrogen). Proteins were then transferred onto a polyvinylidene difluoride membrane (Millipore, Billerica, MA). The membrane was incubated with primary antibodies, followed by horseradish peroxidase-conjugated secondary antibodies. Proteins were visualized using electrochemiluminescence (ECL) detection reagent (GE Healthcare, Milwaukee, WI) and an ImageQuant LAS 4000 digital imaging system (GE Healthcare).

Immunofluorescence

Fixed cells or tissues were permeabilized in 0.2% Triton X-100 for 10 min. After blocking for nonspecific binding in TNB blocking buffer (NEL702, Perkin Elmer,

Norwalk, CT), samples were incubated with primary antibodies, washed three times in PBS with 0.1% Tween-20, and incubated with secondary antibodies described above. Immunofluorescent images were obtained using a confocal microscope LSM700 (Carl Zeiss, Oberkochen, Germany).

Immunohistochemistry

Paraffin-embedded tissue sections were deparaffinized, pretreated with 0.3% H_2O_2 for 30 min, boiled in citrate solution (pH 6.0), and reacted with TNB blocking buffer, anti-PSP1 primary antibody, and biotin-conjugated donkey anti-rabbit IgG secondary antibody (711-066-152, Jackson Immunoresearch, West Grove, PA). Signals were enhanced with the Vectastain ABC kit (Vector Laboratories, Burlingame, CA). Visualization was performed with DAB (Wako, Osaka, Japan) and 1:20,000 dilution of saturated H_2O_2 to observe PSP1 immunopositivity in the nucleus of the motor neuron. The figures were examined using AxioVision imaging software (Carl Zeiss).

Quantitative RT-PCR

Total RNA was extracted from TRIzol reagent-treated samples using an RNAspin Mini RNA Isolation kit (74106, Qiagen, Germantown, MD) after chloroform/phenol extraction [14]. After treatment with DNase I, RT was carried out using Ready-To-Go You-Prime First-Strand Beads (27-9264-01, GE Healthcare) according to the manufacturer's instructions. The resultant cDNA was measured by quantitative PCR with SYBR Premix Ex Taq (Perfect Real Time) (RR041A, Takara) in the Mx3000p system (Stratagene) using Rox as a reference and the following primers: qmNEAT1 FW/RV for mouse NEAT1_1/1_2 cDNA, qmNEAT1_2 FW/RV for mouse NEAT1_2 cDNA, and qmActin FW/RV for mouse β-actin cDNA. All primer sequences are listed in Additional file 8: Table S1. Primers for PCR to detect NEAT1_1 cDNA alone could not be designed; thus, the amount of NEAT1_1 expression was calculated by subtracting the copy number of NEAT 1_2 cDNA from that of total NEAT1 cDNA. The reaction was performed at 95°C for 10 min, followed by 50 cycles at 95°C for 30 s, 60°C for 1 min, and 72°C for 30 s after serial dilutions ranging from 10^{10}, 10^8, 10^6, 10^4, 10^2, to 10^1 copies per 1 μl of DNA solution were prepared as standard samples by subcloning each PCR product into the Zero Blunt TOPO PCR Cloning Kit (K2800, Invitrogen).

EM-ISH

For transmission electron microscopic analysis, frozen sections of the human spinal cord and HeLa cells were used. As mentioned above, *in situ* hybridization with DIG-labeled RNA probes targeting NEAT1_2 or NEAT1_1/1_2 was performed, which included proteinase K digestion at 37°C for 5 min for human tissue sections and 50 s for HeLa cells. Samples were incubated for 72 h at 4°C with mouse anti-DIG (1:250) and rabbit anti-PSP1 (1:250) primary antibodies. Following washes in 0.005% saponin containing 0.1 M phosphate buffer (PB) for 2 h, samples were incubated for 24 h at 4°C with fluorescence- and Nanogold-conjugated anti-mouse secondary antibodies (1:100, Life Technologies) along with fluorescence-conjugated anti-rabbit secondary antibodies (1:800, Life Technologies). After another wash with PB, samples were observed with LSM700. Samples were fixed with 2.5% glutaraldehyde for 10 min at 4°C, followed by 10 min of enhancement with the HQ-Silver kit (Nanoprobes, Stony Brook, NY) in a dark room. After 90 min of additional fixation with 1.0% osmium tetroxide, samples were dehydrated through ethanol, acetone and QY1, and embedded in epon. Ultrathin sections of HeLa cells and motor neurons in the human spinal cord were prepared at a thickness of 70 nm and stained with uranyl acetate and lead citrate for 10 min each. The sections were observed using a JEOL 1230 transmission electron microscope (JEOL, Tokyo, Japan) and photographed with Digital Micrograph 3.3 (Gatan Inc., Warrendale, PA). Sections of 0.5 μm thickness including the spinal ventral horn were simultaneously stained with 0.3% toluidine blue to identify the resected area for observation. Images of toluidine blue staining were examined using AxioVision software (Carl Zeiss).

Statistical analyses

Statistical significance was determined using unpaired Student's *t*-test. $P < 0.05$ was considered statistically significant. Error bars represent the standard deviation of the mean.

Additional files

Additional file 1: Figure S1. Colocalization of endogenous and mutant forms of TDP-43 and FUS/TLS with NEAT1_2 lncRNA. **A.** HeLa cells were double-immunostained with polyclonal antibody against endogenous TDP-43 or FUS/TLS and monoclonal anti-DIG antibody after *in situ* hybridization using DIG-labeled NEAT1_2 probe. Endogenous TDP-43 and FUS/TLS colocalize with NEAT1_2 foci. **B, C.** At 48 hours after transfection with amyotrophic lateral sclerosis (ALS)-linked mutant TDP-43 and FUS/TLS with the V5 tag at the C-terminus, HeLa cells were hybridized with FITC-labeled probe against NEAT1_2 lncRNA, and immunolabeled with monoclonal anti-V5 and polyclonal anti-FITC antibodies. Aggregates formed by mutant TDP-43 and mutant FUS/TLS in the nucleus also overlap with NEAT1_2 foci. The overlapping rate among NEAT1_2 foci with aggregates formed by mutant TDP-43 or mutant FUS/TLS did not differ from that with aggregates formed by wild-type (WT) TDP-43 or FUS/TLS. Data represent mean ± s.d. The frequency was quantitatively evaluated in 50 cells for each transfection. Dotted lines represent the outline of the nucleus. **D.** Characterization of NEAT1_1 foci. Scheme of human NEAT1_1 and NEAT1_2 ncRNAs is shown at the top. Blue bars indicate probe target sites (positions 3,512–5,074 in NEAT1_2 lncRNA sequence for NEAT1_1/1_2 probe and position 14,865–15,472 for NEAT1_2 probe). At 48 hours after transfection with WT TDP-43 and WT FUS/TLS with the V5 tag at the C terminus, fixed HeLa cells were hybridized with FITC-labeled NEAT1_1/1_2 probe and double-labeled with

monoclonal anti-V5 and polyclonal anti-FITC antibodies. Dotted lines represent the outline of the nucleus. Scale bars, 10 μm.

Additional file 2: Figure S2. NEAT1_1 ncRNA is observed in the nuclei of glial cells and motor neurons in the mouse spinal cord by RNA-FISH. Left column: 8-week-old mouse spinal cord; right column: 2-y-old mouse spinal cord. Arrowheads: NEAT1_1 ncRNA in the nuclei of glial cells; arrows: faint labeling of NEAT1_1 ncRNA in the nuclei of motor neurons; dotted line: outline of the nucleus. Asterisks denote lipofuscin with autofluorescence in the cytoplasm. A long-path filter was used to distinguish Hoechst staining from autofluorescence. Scale bars, 10 μm.

Additional file 3: Figure S3. Sense probe designed as a negative control of NEAT1_2 antisense probe in this study. The sense probe was synthesized by using the same template vector as that for the antisense probe against NEAT1_2 lncRNA and a RNA polymerase opposite to that used in synthesis of the antisense probe. Non-specific hybridization with the sense probe was not seen in human motor neurons. * Lipofuscin in the motor neuron. Scale bars, 10 μm.

Additional file 4: Figure S4. NEAT1_2 lncRNA is often colocalized with nuclear PSF and PSP1 in ALS and control cases. RNA-FISH using DIG- or FITC-labeled NEAT1_2 probe in the nuclei of the spinal motor neurons in ALS and control cases. The right-most images show overlaps of NEAT1_2 foci and paraspeckle proteins on orthogonal sections (using ZEN software, Carl Zeiss). Dotted line: outline of the nucleus. Scale bars, 10 μm.

Additional file 5: Figure S5. Occurrence rates of NEAT1_2 lncRNA foci in all stages of ventral motor neurons in ALS and control cases. Totally without classification, there was no difference in occurrence rates of NEAT1_2 lncRNA in all stages of motor neurons between in ALS and control cases (40.2 ± 15.5 % vs. 35.1 ± 22.6 %, respectively, $P=0.328$).

Additional file 6: Figure S6. A. Electron microscopic observations combined with *in situ* hybridization (EM-ISH) in the nuclei of human spinal motor neurons using the NEAT1_1/1_2 probe (ALS and control). Using the NEAT1_1/1_2 probe, both the halo pattern of aggregation (arrows in b, e, f) and the other pattern of aggregates extending into the central portion are observed in an ALS case (a, b) and HeLa cells (e, f). Meanwhile, the halo-shaped accumulation pattern is hardly observed in a control case (c, d). HeLa cells are used as a positive control for paraspeckle formation. Scale bars, 500 nm (a, b, e, f) and 200 nm (c, d). **B**. Electron microscopic observations in a HeLa cell using diluted NEAT1_1/1_2 probe. Even when diluted NEAT1_1/1_2 probe is used, both central (a) and halo-like (b) patterns of aggregation are observed in a HeLa cell. This suggests that NEAT1_1 RNA may show the central accumulation pattern independently of the IGAZ margin. The lower panels are magnified images of the (a) and (b) regions. Scale bars, 5 μm (upper) and 200 nm (lower, a and b). **C**. EM-ISH observations in a spinal motor neuron of another case of ALS (Pt C) using the NEAT1_2 probe. Another case of ALS also shows halo-like patterns of aggregation labeled with the NEAT1_2 probe in a spinal motor neuron, similar to Pt B in Figure 6B-a and -b. Scale bars, 100 nm.

Additional file 7: Figure S7. Prediction of FUS/TLS- and TDP-43-binding sites in NEAT1 ncRNA. Black arrowheads represent the positions (3,440–3,460; 10,108–10,127; and 18,316–18,335) where the proposed binding sites similar to the *SON* cluster are located in the NEAT1_2 genome, predicted by PAR-CLIP as preferred binding sites of FUS/TLS (ref. [27] in the text). Screening was carried out under the conditions of stem size = 6 bp and loop size = 7–9 nucleotides. Green nucleotides comprise conventional stem structures, and red nucleotides represent typical non-Watson-Crick base pairs proposed for the *SON* cluster. The yellow boxes (in positions 6,662–6,728 and 21,464–21,544) represent the binding sites of TDP-43, which have been predicted by TDP-43 iCLIP in a previous report (ref. [23] in the text).

Additional file 8: Table S1. Oligonucleotides used in this study.

Abbreviations
lncRNA: long non-coding RNA; ncRNA: non-coding RNA; NEAT: nuclear-enriched abundant transcript; TDP-43: TAR DNA-binding protein-43; FUS/TLS: fused in sarcoma/translocated in liposarcoma; ALS: amyotrophic lateral sclerosis; ISH: *in situ* hybridization; WT: wild-type; CLIP: UV cross-linking and immunoprecipitation; IGAZ: interchromatin granule-associated zone; PSP1: paraspeckle protein-1; PSF: polypyrimidine tract binding protein-

associated splicing factor; RT: reverse transcription; PCR: polymerase chain reaction; RNA-FISH: *in situ* hybridization followed by fluorescent immunohistochemistry; EM-ISH: electron microscopic analysis combined with *in situ* hybridization; ASO: antisense oligonucleotide; FITC: fluorescein isothiocyanate; DIG: digoxigenin.

Competing interests
H. Okano is the scientific consultant of San Bio, Inc; Eisai Co Ltd; and Daiichi Sankyo Co Ltd. K. The remaining authors declare no competing financial interests. The authors declare that they have no competing interests.

Authors' contributions
YN, SN and SS performed all the experiments. YN, SN, TH, HJO and HO designed the experiments. TH and SN developed the RNA probes for *in situ* hybridization and TH generated rabbit polyclonal anti-PSP1 antibody. MT and SM collected to store the human spinal cords and MT provided them in appropriate conditions. SS, KK, TI provided technical assistance in immunostaining and microscopic observation. YN, SN, HJO, MT, SM, NS and HO contributed to the approvals of the Ethics Committees of institutes associated with this study. All authors contributed to the preparation of the manuscript. All authors read and approved the final manuscript.

Author details
[1]Department of Physiology, School of Medicine, Keio University, 35 Shinanomachi, Shinjuku-ku, Tokyo 160-8582, Japan. [2]Department of Neurology, School of Medicine, Keio University, 35 Shinanomachi, Shinjuku-ku, Tokyo 160-8582, Japan. [3]RNA Biology Laboratory, RIKEN Advanced Science Institute, 2-1 Hirosawa, Saitama 351-0198, Japan. [4]Genomic Neo-Function Research Group, Biomedical Research Institute, National Institute of Advanced Industrial Science and Technology (AIST), 2-4-7 Aomi, Koutou-ku, Tokyo 135-0064, Japan. [5]Division of Regenerative Medicine, Jikei University School of Medicine, 3-25-8 Nishi-Shinbashi, Minato-ku, Tokyo 105-8461, Japan. [6]Institute of Brain and Blood Vessels, Mihara Memorial Hospital, 366 Ohtacho, Isesaki, Gunma 372-0006, Japan. [7]Tokyo Metropolitan Geriatric Hospital & Institute of Gerontology, 35-2 Sakaecho, Itabashi, Tokyo 173-0015, Japan.

References
1. Chio A, Calvo A, Moglia C, Gamna F, Mattei A, Mazzini L, Mora G, Parals: **Non-invasive ventilation in amyotrophic lateral sclerosis: a 10 year population based study.** *J Neurol Neurosurg Psychiatry* 2012, **83**:377–381.
2. Kabashi E, Valdmanis PN, Dion P, Spiegelman D, McConkey BJ, Vande Velde C, Bouchard JP, Lacomblez L, Pochigaeva K, Salachas F, Pradat PF, Camu W, Meininger V, Dupre N, Rouleau GA: **TARDBP mutations in individuals with sporadic and familial amyotrophic lateral sclerosis.** *Nat Genet* 2008, **40**:572–574.
3. DeJesus-Hernandez M, Mackenzie IR, Boeve BF, Boxer AL, Baker M, Rutherford NJ, Nicholson AM, Finch NA, Flynn H, Adamson J, Kouri N, Wojtas A, Sengdy P, Hsiung GY, Karydas A, Seeley WW, Josephs KA, Coppola G, Geschwind DH, Wszolek ZK, Feldman H, Knopman DS, Petersen RC, Miller BL, Dickson DW, Boylan KB, Graff-Radford NR, Rademakers R: **Expanded**

GGGGCC hexanucleotide repeat in noncoding region of C9ORF72 causes chromosome 9p-linked FTD and ALS. *Neuron* 2011, 72:245–256.

4. Kwiatkowski TJ Jr, Bosco DA, Leclerc AL, Tamrazian E, Vanderburg CR, Russ C, Davis A, Gilchrist J, Kasarskis EJ, Munsat T, Valdmanis P, Rouleau GA, Hosler BA, Cortelli P, de Jong PJ, Yoshinaga Y, Haines JL, Pericak-Vance MA, Yan J, Ticozzi N, Siddique T, McKenna-Yasek D, Sapp PC, Horvitz HR, Landers JE, Brown RH Jr: Mutations in the FUS/TLS gene on chromosome 16 cause familial amyotrophic lateral sclerosis. *Science* 2009, 323:1205–1208.

5. Vance C, Rogelj B, Hortobagyi T, De Vos KJ, Nishimura AL, Sreedharan J, Hu X, Smith B, Ruddy D, Wright P, Ganesalingam J, Williams KL, Tripathi V, Al-Saraj S, Al-Chalabi A, Leigh PN, Blair IP, Nicholson G, De Belleroche J, Gallo JM, Miller CC, Shaw CE: Mutations in FUS, an RNA processing protein, cause familial amyotrophic lateral sclerosis type 6. *Science* 2009, 323:1208–1211.

6. Maruyama H, Morino H, Ito H, Izumi Y, Kato H, Watanabe Y, Kinoshita Y, Kamada M, Nodera H, Suzuki H, Komure O, Matsuura S, Kobatake K, Morimoto N, Abe K, Suzuki N, Aoki M, Kawata A, Hirai T, Kato T, Ogasawara K, Hirano A, Takumi T, Kusaka H, Hagiwara K, Kaji R, Kawakami H: Mutations of optineurin in amyotrophic lateral sclerosis. *Nature* 2010, 465:223–226.

7. Fecto F, Yan J, Vemula SP, Liu E, Yang Y, Chen W, Zheng JG, Shi Y, Siddique N, Arrat H, Donkervoort S, Ajroud-Driss S, Sufit RL, Heller SL, Deng HX, Siddique T: SQSTM1 mutations in familial and sporadic amyotrophic lateral sclerosis. *Arch Neurol* 2011, 68:1440–1446.

8. Nishimoto Y, Ito D, Yagi Y, Nihei Y, Tsunoda Y, Suzuki N: Characterization of alternative isoforms and inclusion body of the TAR DNA-binding protein-43. *J Biol Chem* 2010, 285:608–619.

9. Ito D, Seki M, Tsunoda Y, Uchiyama H, Suzuki N: Nuclear transport impairment of amyotrophic lateral sclerosis-linked mutations in FUS/TLS. *Ann Neurol* 2011, 69:152–162.

10. Nishimoto Y, Okano HJ, Imai T, Poole AJ, Suzuki N, Keirstead HS, Okano H: Cellular toxicity induced by the 26-kDa fragment and amyotrophic lateral sclerosis (ALS)-associated mutant forms of TDP-43 in human embryonic stem cell-derived motor neurons. *NeurologyClin Neurosci* 2013, 1:24–31.

11. Arai T, Hasegawa M, Akiyama H, Ikeda K, Nonaka T, Mori H, Mann D, Tsuchiya K, Yoshida M, Hashizume Y, Oda T: TDP-43 is a component of ubiquitin-positive tau-negative inclusions in frontotemporal lobar degeneration and amyotrophic lateral sclerosis. *Biochem Biophys Res Commun* 2006, 351:602–611.

12. Neumann M, Sampathu DM, Kwong LK, Truax AC, Micsenyi MC, Chou TT, Bruce J, Schuck T, Grossman M, Clark CM, McCluskey LF, Miller BL, Masliah E, Mackenzie IR, Feldman H, Feiden W, Kretzschmar HA, Trojanowski JQ, Lee VM: Ubiquitinated TDP-43 in frontotemporal lobar degeneration and amyotrophic lateral sclerosis. *Science* 2006, 314:130–133.

13. Polymenidou M, Lagier-Tourenne C, Hutt KR, Bennett CF, Cleveland DW, Yeo GW: Misregulated RNA processing in amyotrophic lateral sclerosis. *Brain Res* 2012, 1462:3–15.

14. Kawahara Y, Ito K, Sun H, Aizawa H, Kanazawa I, Kwak S: Glutamate receptors: RNA editing and death of motor neurons. *Nature* 2004, 427:801.

15. Chen LL, Carmichael GG: Altered nuclear retention of mRNAs containing inverted repeats in human embryonic stem cells: functional role of a nuclear noncoding RNA. *Mol Cell* 2009, 35:467–478.

16. Prasanth KV, Prasanth SG, Xuan Z, Hearn S, Freier SM, Bennett CF, Zhang MQ, Spector DL: Regulating gene expression through RNA nuclear retention. *Cell* 2005, 123:249–263.

17. Bond CS, Fox AH: Paraspeckles: nuclear bodies built on long noncoding RNA. *J Cell Biol* 2009, 186:637–644.

18. Clemson CM, Hutchinson JN, Sara SA, Ensminger AW, Fox AH, Chess A, Lawrence JB: An architectural role for a nuclear noncoding RNA: NEAT1 RNA is essential for the structure of paraspeckles. *Mol Cell* 2009, 33:717–726.

19. Sasaki YT, Ideue T, Sano M, Mituyama T, Hirose T: MENepsilon/beta noncoding RNAs are essential for structural integrity of nuclear paraspeckles. *Proc Natl Acad Sci USA* 2009, 106:2525–2530.

20. Sunwoo H, Dinger ME, Wilusz JE, Amaral PP, Mattick JS, Spector DL: MEN epsilon/beta nuclear-retained non-coding RNAs are up-regulated upon muscle differentiation and are essential components of paraspeckles. *Genome Res* 2009, 19:347–359.

21. Hutchinson JN, Ensminger AW, Clemson CM, Lynch CR, Lawrence JB, Chess A: A screen for nuclear transcripts identifies two linked noncoding RNAs associated with SC35 splicing domains. *BMC Genomics* 2007, 8:39.

22. Guru SC, Agarwal SK, Manickam P, Olufemi SE, Crabtree JS, Weisemann JM, Kester MB, Kim YS, Wang Y, Emmert-Buck MR, Liotta LA, Spiegel AM, Boguski MS, Roe BA, Collins FS, Marx SJ, Burns L, Chandrasekharappa SC: A transcript map for the 2.8-Mb region containing the multiple endocrine neoplasia type 1 locus. *Genome Res* 1997, 7:725–735.

23. Tollervey JR, Curk T, Rogelj B, Briese M, Cereda M, Kayikci M, Konig J, Hortobagyi T, Nishimura AL, Zupunski V, Patani R, Chandran S, Rot G, Zupan B, Shaw CE, Ule J: Characterizing the RNA targets and position-dependent splicing regulation by TDP-43. *Nat Neurosci* 2011, 14:452–458.

24. Wang X, Arai S, Song X, Reichart D, Du K, Pascual G, Tempst P, Rosenfeld MG, Glass CK, Kurokawa R: Induced ncRNAs allosterically modify RNA-binding proteins in cis to inhibit transcription. *Nature* 2008, 454:126–130.

25. Rogelj B, Easton LE, Bogu GK, Stanton LW, Rot G, Curk T, Zupan B, Sugimoto Y, Modic M, Haberman N, Tollervey J, Fujii R, Takumi T, Shaw CE, Ule J: Widespread binding of FUS along nascent RNA regulates alternative splicing in the brain. *Sci Rep* 2012, 2:603.

26. Lagier-Tourenne C, Polymenidou M, Hutt KR, Vu AQ, Baughn M, Huelga SC, Clutario KM, Ling SC, Liang TY, Mazur C, Wancewicz E, Kim AS, Watt A, Freier S, Hicks GG, Donohue JP, Shiue L, Bennett CF, Ravits J, Cleveland DW, Yeo GW: Divergent roles of ALS-linked proteins FUS/TLS and TDP-43 intersect in processing long pre-mRNAs. *Nat Neurosci* 2012, 15:1488–1497.

27. Hoell JI, Larsson E, Runge S, Nusbaum JD, Duggimpudi S, Farazi TA, Hafner M, Borkhardt A, Sander C, Tuschl T: RNA targets of wild-type and mutant FET family proteins. *Nat Struct Mol Biol* 2011, 18:1428–1431.

28. Cardinale S, Cisterna B, Bonetti P, Aringhieri C, Biggiogera M, Barabino SM: Subnuclear localization and dynamics of the Pre-mRNA 3' end processing factor mammalian cleavage factor I 68-kDa subunit. *Mol Biol Cell* 2007, 18:1282–1292.

29. Souquere S, Beauclair G, Harper F, Fox A, Pierron G: Highly ordered spatial organization of the structural long noncoding NEAT1 RNAs within paraspeckle nuclear bodies. *Mol Biol Cell* 2010, 21:4020–4027.

30. Visa N, Puvion-Dutilleul F, Bachellerie JP, Puvion E: Intranuclear distribution of U1 and U2 snRNAs visualized by high resolution in situ hybridization: revelation of a novel compartment containing U1 but not U2 snRNA in HeLa cells. *Eur J Cell Biol* 1993, 60:308–321.

31. Fox AH, Lam YW, Leung AK, Lyon CE, Andersen J, Mann M, Lamond AI: Paraspeckles: a novel nuclear domain. *Curr Biol* 2002, 12:13–25.

32. Mao YS, Sunwoo H, Zhang B, Spector DL: Direct visualization of the co-transcriptional assembly of a nuclear body by noncoding RNAs. *Nat Cell Biol* 2011, 13:95–101.

33. Naganuma T, Nakagawa S, Tanigawa A, Sasaki YF, Goshima N, Hirose T: Alternative 3'-end processing of long noncoding RNA initiates construction of nuclear paraspeckles. *EMBO J* 2012, 31:4020–4034.

34. Shevtsov SP, Dundr M: Nucleation of nuclear bodies by RNA. *Nat Cell Biol* 2011, 13:167–173.

35. Wang IF, Reddy NM, Shen CK: Higher order arrangement of the eukaryotic nuclear bodies. *Proc Natl Acad Sci USA* 2002, 99:13583–13588.

36. Nakagawa S, Naganuma T, Shioi G, Hirose T: Paraspeckles are subpopulation-specific nuclear bodies that are not essential in mice. *J Cell Biol* 2011, 193:31–39.

37. Ross OA, Rutherford NJ, Baker M, Soto-Ortolaza AI, Carrasquillo MM, DeJesus-Hernandez M, Adamson J, Li M, Volkening K, Finger E, Seeley WW, Hatanpaa KJ, Lomen-Hoerth C, Kertesz A, Bigio EH, Lippa C, Woodruff BK, Knopman DS, White CL 3rd, Van Gerpen JA, Meschia JF, Mackenzie IR, Boylan K, Boeve BF, Miller BL, Strong MJ, Uitti RJ, Younkin SG, Graff-Radford NR, Petersen RC, et al: Ataxin-2 repeat-length variation and neurodegeneration. *Hum Mol Genet* 2011, 20:3207–3212.

38. Dammer EB, Fallini C, Gozal YM, Duong DM, Rossoll W, Xu P, Lah JJ, Levey AI, Peng J, Bassell GJ, Seyfried NT: Coaggregation of RNA-binding proteins in a model of TDP-43 proteinopathy with selective RGG motif methylation and a role for RRM1 ubiquitination. *PLoS One* 2012, 7:e38658.

39. Tan AY, Manley JL: TLS inhibits RNA polymerase III transcription. *Mol Cell Biol* 2010, 30:186–196.

40. Xie SQ, Martin S, Guillot PV, Bentley DL, Pombo A: Splicing speckles are not reservoirs of RNA polymerase II, but contain an inactive form, phosphorylated on serine2 residues of the C-terminal domain. *Mol Biol Cell* 2006, 17:1723–1733.

41. Kaneko S, Rozenblatt-Rosen O, Meyerson M, Manley JL: The multifunctional protein p54nrb/PSF recruits the exonuclease XRN2 to facilitate pre-mRNA 3' processing and transcription termination. *Genes Dev* 2007, 21:1779–1789.

42. Hoque M, Ji Z, Zheng D, Luo W, Li W, You B, Park JY, Yehia G, Tian B: Analysis of alternative cleavage and polyadenylation by 3' region extraction and deep sequencing. *Nat Methods* 2013, **10**:133–139.
43. Arnold ES, Ling SC, Huelga SC, Lagier-Tourenne C, Polymenidou M, Ditsworth D, Kordasiewicz HB, McAlonis-Downes M, Platoshyn O, Parone PA, Da Cruz S, Clutario KM, Swing D, Tessarollo L, Marsala M, Shaw CE, Yeo GW, Cleveland DW: ALS-linked TDP-43 mutations produce aberrant RNA splicing and adult-onset motor neuron disease without aggregation or loss of nuclear TDP-43. *Proc Natl Acad Sci USA* 2013, **110**:E736–745.
44. Wu SC, Kallin EM, Zhang Y: Role of H3K27 methylation in the regulation of lncRNA expression. *Cell Res* 2010, **20**:1109–1116.
45. Ishigaki S, Masuda A, Fujioka Y, Iguchi Y, Katsuno M, Shibata A, Urano F, Sobue G, Ohno K: Position-dependent FUS-RNA interactions regulate alternative splicing events and transcriptions. *Sci Rep* 2012, **2**:529.
46. Zhang C, Darnell RB: Mapping in vivo protein-RNA interactions at single-nucleotide resolution from HITS-CLIP data. *Nat Biotechnol* 2011, **29**:607–614.
47. Nishimoto Y, Yamashita T, Hideyama T, Tsuji S, Suzuki N, Kwak S: Determination of editors at the novel A-to-I editing positions. *Neurosci Res* 2008, **61**:201–206.
48. Raj B, O'Hanlon D, Vessey JP, Pan Q, Ray D, Buckley NJ, Miller FD, Blencowe BJ: Cross-regulation between an alternative splicing activator and a transcription repressor controls neurogenesis. *Mol Cell* 2011, **43**:843–850.
49. Ule J, Jensen K, Mele A, Darnell RB: CLIP: a method for identifying protein-RNA interaction sites in living cells. *Methods* 2005, **37**:376–386.

PML mediates glioblastoma resistance to mammalian target of rapamycin (mTOR)-targeted therapies

Akio Iwanami[a], Beatrice Gini[b,c,1], Ciro Zanca[b,1], Tomoo Matsutani[b], Alvaro Assuncao[d], Ali Nael[e], Julie Dang[f], Huijun Yang[b], Shaojun Zhu[g], Jun Kohyama[g], Issay Kitabayashi[h], Webster K. Cavenee[b,i], Timothy F. Cloughesy[j], Frank B. Furnari[b,i,k], Masaya Nakamura[a], Yoshiaki Toyama[a], Hideyuki Okano[l], and Paul S. Mischel[b,i,k,2]

Departments of [a]Orthopaedic Surgery and [l]Physiology, Keio University School of Medicine, Tokyo 160-8582, Japan; [b]Ludwig Institute for Cancer Research, [i]Moores Comprehensive Cancer Center, and [k]Department of Pathology, University of California at San Diego, La Jolla, CA 92093; [c]Department of Neurological, Neuropsychological, Morphological and Movement Sciences, University of Verona, 37134 Verona, Italy; [d]Undergraduate Minor in Biomedical Research Program, and Departments of [g]Molecular and Medical Pharmacology and [j]Neurology, University of California, Los Angeles, CA 90095; [e]Department of Pathology, University of California, Irvine, CA 92697; [f]School of Pharmacy, University of California, San Francisco, CA 94104; and [h]Division of Hematological Malignancy, National Cancer Center Research Institute, Tokyo 104-0045, Japan

Despite their nearly universal activation of mammalian target of rapamycin (mTOR) signaling, glioblastomas (GBMs) are strikingly resistant to mTOR-targeted therapy. We analyzed GBM cell lines, patient-derived tumor cell cultures, and clinical samples from patients in phase 1 clinical trials, and find that the promyelocytic leukemia (PML) gene mediates resistance to mTOR-targeted therapies. Direct mTOR inhibitors and EGF receptor (EGFR) inhibitors that block downstream mTOR signaling promote nuclear PML expression in GBMs, and genetic overexpression and knockdown approaches demonstrate that PML prevents mTOR and EGFR inhibitor-dependent cell death. Low doses of the PML inhibitor, arsenic trioxide, abrogate PML expression and reverse mTOR kinase inhibitor resistance in vivo, thus markedly inhibiting tumor growth and promoting tumor cell death in mice. These results identify a unique role for PML in mTOR and EGFR inhibitor resistance and provide a strong rationale for a combination therapeutic strategy to overcome it.

mTORC1 | glioma

Glioblastoma (GBM) is the most common malignant primary brain tumor of adults and one of the most lethal forms of cancer (1, 2). As a consequence of frequent EGF receptor (EGFR) amplification and/or activating mutation, other receptor tyrosine kinase amplifications and phosphatase and tensin homolog (PTEN) loss (3, 4), persistent hyperactivation of the phosphatidyl-inositol-3-kinase (PI3K) pathway is observed in nearly 90% of GBMs making the downstream effector, mammalian target of rapamycin (mTOR), a compelling drug target. mTOR links growth factor signaling through PI3K to energy and nutrient status, protein translation, autophagy, and tumor cell metabolism (5). Thus, mTOR is a critical integrator that regulates tumor growth, survival and, potentially, cancer drug resistance.

The allosteric mTOR inhibitor rapamycin has failed in the clinic as a treatment for GBM patients. We previously reported that in a clinical phase I trial for patients with recurrent PTEN-deficient GBM, rapamycin treatment led to Akt activation resulting in loss of negative feedback, consistent with the homeostatic regulatory role of mTOR complex I (mTORC1) as a negative regulator of PI3K/Akt signaling (6). Further, we demonstrated a critical role for mTOR complex II (mTORC2) as a critical mediator of rapamycin resistance through Akt and mTORC1-independent signaling pathways (7). These results have highlighted the potential role for mTOR kinase inhibitors, which block both mTOR signaling complexes, in the treatment of GBM and potentially other cancers.

The interconnectivity between mTOR signaling complexes suggests the possibility that multiple mechanisms of mTOR inhibitor resistance may exist, some of which may be clinically actionable. The promyelocytic leukemia (PML) gene may represent one such mechanism. PML is a pleiotropic tumor suppressor that plays multiple roles on cellular homeostasis such as apoptosis, proliferation, and senescence (8, 9). PML, as part of

the retinoic acid receptor (RAR)/PML fusion protein identified in acute promyelocytic leukemia, represents one of the first molecular cancer targets amenable to targeted drug therapy (10, 11). Although the loss of PML protein expression is associated with tumor progression in many tumors (12), some tumors show paradoxically high levels of PML. For example, PML has been shown to be highly expressed in hematopoetic stem cells and in chemotherapy resistant, quiescent leukemia-initiating CML cells (13).

PML is also closely related to receptor tyrosine kinase (RTK)/PI3K/Akt/mTOR signaling pathway at multiple levels. PML has been reported to oppose the function of nuclear Akt (14) and was also identified as a repressor of mTOR through inhibition of Ras homolog enriched in brain (Rheb)–mTOR interaction during hypoxia (15). Further, PML is responsible for the repression of transcriptional activity from the EGFR promoter (16). Considering these factors, we hypothesized that PML might promote resistance to rapamycin, ATP-competitive mTOR kinase inhibitors, and EGFR tyrosine kinase inhibitors by controlling RTK/PI3K/Akt/mTOR signaling and cell cycle in GBM. Here, we examine the expression of PML in GBM cell lines and GBM-patient tissues; show that it is regulated by PI3K/Akt/mTOR signaling; demonstrate the impact of mTOR inhibition on PML expression; and then, using genetic and pharmacological approaches and correlations from clinical samples of patients treated with rapamycin or erlotinib, demonstrate a role for PML in preventing drug-induced apoptosis and promoting clinical resistance. Finally, we identify genetic and pharmacological approaches to overcome this drug resistance.

Results

PML Expression in GBM Patients. To examine the expression of PML in GBM patients, we performed immunohistochemical analysis of GBM by using a tissue microarray (TMA) consisting of multiple representative regions of tumor and adjacent normal tissue from 87 patients with primary GBMs (17, 18). Expression of PML, Ki-67, and phospho-S6 was analyzed and scored independently by two neuropathologists as high or low (scoring summarized in Fig. 1 A and B). PML was highly expressed in 41.4% of tumor samples (Fig. 1 A and B), and the expression was

A

	Ki-67 high	Ki-67 low
PML high	14	22
PML low	45	6

r = -0.5202198, P < 0.01

B

	p-S6 high	p-S6 low
PML high	11	25
PML low	38	13

r = -0.4500150, P < 0.01
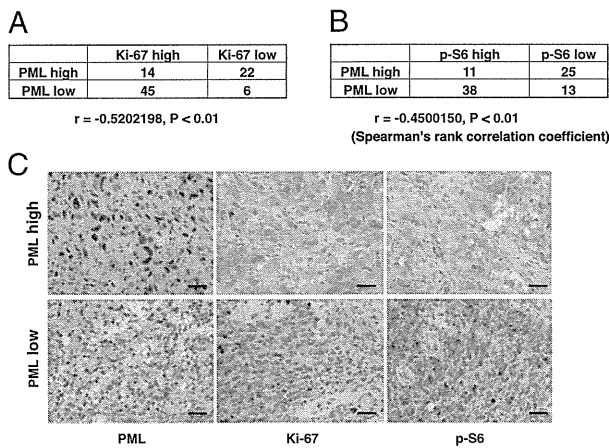(Spearman's rank correlation coefficient)

C

Fig. 1. PML is inversely correlated with proliferation rate and mTOR signaling in GBM clinical samples. (A and B) Tissue microarrays containing tumor samples from 87 GBM patients were stained by using PML, Ki-67, and p-S6 antibody, respectively. PML is highly expressed in 40% of GBM patients. Correlation analyses show PML significantly inversely correlate with Ki-67 (A) and p-S6 (B). (C) Immunohistochemical staining of (reddish brown) PML, Ki-67, and p-S6 from a representative GBM patient. (Magnification: 10×.) Nuclei were counterstained with hematoxylin (blue). (Scale bar: 100 μm.)

significantly inversely correlated with the cell proliferation marker Ki-67 (Fig. 1 A and C; $r = -0.52$, $P < 0.01$) and with mTORC1 signaling, as measured by S6 phosphorylation (Fig. 1 B and C; $r = -0.45$, $P < 0.01$).

Rapamycin Induces Expression and Nuclear Aggregation of PML.

Next, we treated GBM cells and a GBM patient-derived cell culture with rapamycin to determine the effect of RTK/PI3K/mTOR inhibitor on PML (Fig. 2 A–C). Exposure to rapamycin treatment, or the ATP-competitive mTOR kinase inhibitor pp242, at doses sufficient to inhibit mTORC1 signaling, led to time-dependent increases in PML expression (Fig. 2 and Fig. S1). The EGFR tyrosine kinase inhibitor, erlotinib, which inhibited mTORC1 signaling downstream of EGFR, similarly elevated PML expression (Fig. 2B). Biochemical results were confirmed by fluorescent immunocytochemical analyses, demonstrating strongly granular patterns of PML staining in the nucleus, consistent with its reported distribution (Fig. 2C).

Overexpression of PML Contributes to Decreasing PI3K/Akt/mTOR Signaling and a Slower Cell Cycle.

We hypothesized that PML might contribute to rapamycin, mTOR kinase inhibitor, and/or EGFR tyrosine kinase inhibitor resistance in GBM. Therefore, we performed retroviral transduction of PML I into U87 cells and examined the effect on PI3K/Akt/mTOR signaling and cell cycle progression. First, we performed double-immunofluorescent staining with PML and HA tag to confirm the overexpression of PML I (Fig. 3A). Compared with control, the retroviral-infected U87 cells expressed exogenous PML in both their nuclei and cytoplasm. Immunoblot analyses of these lysates demonstrated the increased expression of all PML isoforms, which would result from alternative splicing of the longest form, PML I (9). After confirmation of PML overexpression in these cell lines, we examined several PI3K/Akt/mTOR signaling proteins and cell cycle–related proteins by Western blotting. Akt and S6 phosphorylation were significantly decreased in U87 GBM cells that exogenously expressed PML I. Moreover, the cell cycle related proteins, cyclin D1 and cyclin-dependent kinase inhibitor 1 (p21), were also notably decreased, suggesting that PML contributes to decreasing PI3K/Akt/mTOR signaling and slowing down the cell cycle (Fig. 3B). We further performed cell proliferation assays by using these

cell lines and confirmed that U87PML I cells were significantly less proliferative than control U87 cells (Fig. 3C; $**P < 0.01$).

Flow cytometric cell cycle analyses demonstrated an increased G1 fraction in U87PML I-expressing GBM cells (Fig. 3D; $**P < 0.01$). To determine whether this conferred rapamycin resistance, we treated U87PML I cells and control cells with rapamycin for 48 h and analyzed the drug effect by using WST-1 assays. PML I overexpression significantly reduced the growth inhibitory effect of rapamycin (Fig. 3E; $**P < 0.01$).

Interfering RNA-Mediated PML Knockdown Sensitizes GBM Cell Lines to mTOR and EGFR Kinase Inhibitor Treatment.

To confirm a specific role for PML in preventing mTOR and EGFR-kinase inhibitor-dependent cell death, we induced small interfering RNAs (siRNA)-mediated PML knockdown in multiple GBM cell lines and assessed its impact on response to rapamycin, pp242, and erlotinib. TUNEL analysis demonstrated that PML knockdown significantly sensitized all of the GBM cell lines to pp242 and erlotinib-mediated cell death (Fig. 4 A and B; $*P < 0.05$, $**P < 0.01$), which was confirmed by analysis of polyADP ribose polymerase (PARP) cleavage (Fig. S2). Of note, in contrast to pp242, rapamycin, which has less activity against mTORC2 than does pp242, induced minimal cell death even in the presence of PML knockdown, potentially suggesting a role for sustained mTORC2 signaling in mediating survival (7). Taken together, these data demonstrate that PML contributes to mTOR and EGFR kinase inhibitor resistance in GBM by suppressing tumor cell death, which can be reversed by pharmacological or genetic inhibition of PML.

As₂O₃ Abrogates pp242-Induced PML Up-Regulation and Sensitizes GBMs to mTOR Kinase Inhibitor-Mediated Cell Death.

Arsenic trioxide (As_2O_3) has long been used as a therapeutic agent for promyelocytic leukemia (19–21). Besides its cell toxicity, As_2O_3 has been shown to target PML for degradation through a sumoylation-dependent process leading to PML polyubiquitination and proteosomal degradation (11, 13, 22–24). Therefore, we investigated the effect of As_2O_3 on reduction of PML in U87 cells. Single As_2O_3 treatments reduced PML expression at both low (0.15 μM) and high concentrations (2 μM) and decreased proliferation in serum-containing growth condition (Fig. S3 A and B). Notably, a high concentration (2 μM) induced an increase in p53 levels and decreased levels of cyclin D1 expression (Fig. S3A). The ability of low dose As_2O_3 to inhibit proliferation in the absence of p53 induction is consistent with previous papers (13, 25)
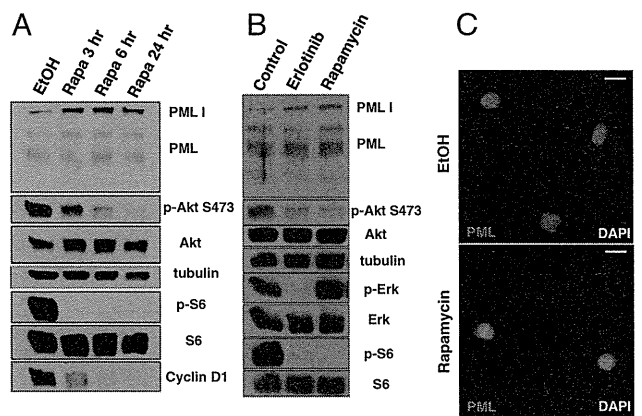

Fig. 2. PI3K/Akt/mTOR inhibitors induce PML expression in GBM cells. (A) Western blot analysis of the effect of rapamycin treatment on PML expression in U87 cells. Cells are cultured in serum-free condition. (B) Effect of the EGFR inhibitor erlotinib and rapamycin on PML expression in GBM patient-derived cells. Cells are cultured under neurosphere conditions. (C) Immunofluorescence of PML (red) in U87 cells treated with rapamycin or control. Nuclei are stained with DAPI (blue). (Scale bar: 20 μm.)
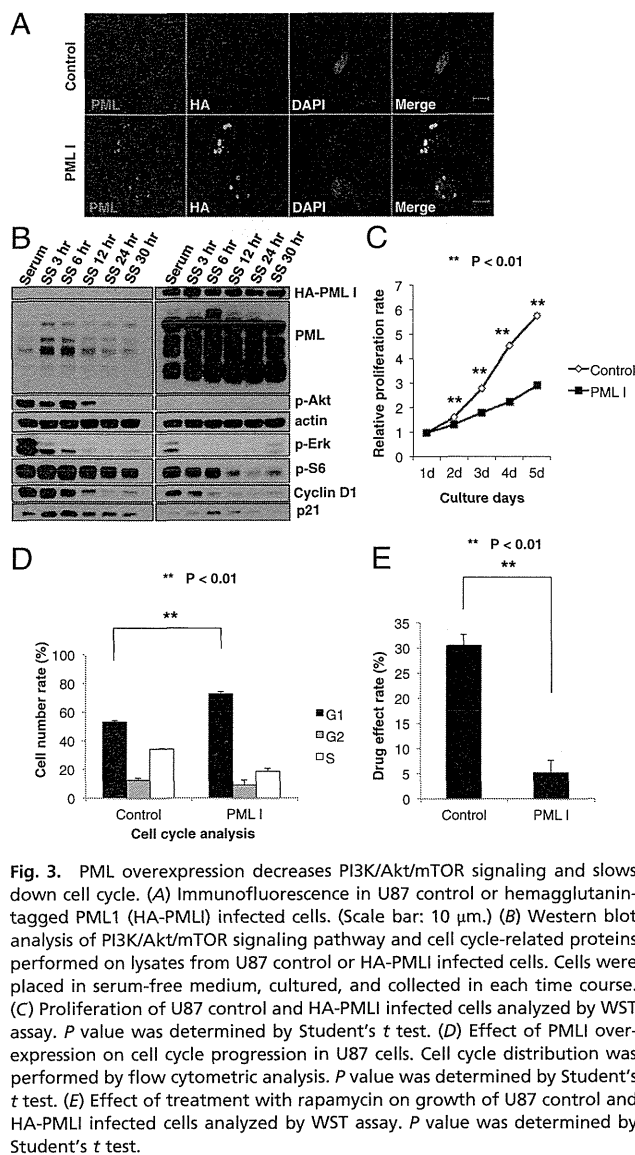
Iwanami et al.

− 50 −

Fig. 3. PML overexpression decreases PI3K/Akt/mTOR signaling and slows down cell cycle. (A) Immunofluorescence in U87 control or hemagglutanin-tagged PML1 (HA-PMLI) infected cells. (Scale bar: 10 μm.) (B) Western blot analysis of PI3K/Akt/mTOR signaling pathway and cell cycle-related proteins performed on lysates from U87 control or HA-PMLI infected cells. Cells were placed in serum-free medium, cultured, and collected in each time course. (C) Proliferation of U87 control and HA-PMLI infected cells analyzed by WST assay. P value was determined by Student's t test. (D) Effect of PMLI overexpression on cell cycle progression in U87 cells. Cell cycle distribution was performed by flow cytometric analysis. P value was determined by Student's t test. (E) Effect of treatment with rapamycin on growth of U87 control and HA-PMLI infected cells analyzed by WST assay. P value was determined by Student's t test.

suggesting that lower concentration of As_2O_3 mediates its effect by reducing PML levels and not by inducing DNA damage. Neither pp242, nor As_2O_3 alone, promoted extensive tumor cell death. In contrast, As_2O_3 (0.15 μM) significantly and synergistically promoted pp242- dependent apoptotic cell death, as measured by cleaved caspase and TUNEL staining, independent of any effect on p53 phosphorylation (*$P < 0.01$; Fig. 5 A and B and Fig. S3C).

Therefore, we analyzed the effect of combining the mTOR kinase inhibitor pp242 with As_2O_3 on PML expression, cell death, and tumor size in U87 GBM xenografts (Fig. 5 C–F). Sixteen days of treatment with pp242 and As_2O_3, significantly reduced the growth of GBMs by nearly threefold ($P < 0.0005$) and induced TUNEL-positive cell death, an effect that was not detected with either pp242 or As_2O_3 monotherapy (Fig. 5 C, D, and F). Importantly, As_2O_3 also abrogated the pp242-mediated up-regulation of PML expression (Fig. 5E). Ki-67 staining was also diminished, although the decrease failed to reach statistical significance (Fig. S4). Taken together, these results demonstrate that As_2O_3 dramatically synergizes with mTOR kinase inhibition to promote GBM cell death and block tumor growth in vivo.

Immunohistochemical Analyses of PML Expression in GBM Patients Treated with Rapamycin or Erlotinib. Finally, to establish clinical relevance and to determine whether PML up-regulation is associated with mTOR and EGFR inhibitor resistance in GBM patients, we performed immunohistochemical analyses of tumor samples obtained from two "biopsy-treat-biopsy" paradigm phase I clinical trials, for which tumor tissue was obtained 7–10 d after treatment with rapamycin or lapatinib (details presented in refs. 6 and 26). As shown in Fig. 6, rapamycin (Fig. 6 A and B) and erlotinib (Fig. 6 C and D) treatment were both associated with significantly enhanced nuclear PML expression (*$P < 0.01$).

Discussion

PML is a pleiotropic tumor suppressor protein that is lost in many cancer types (12, 27). PML negatively regulates Akt-mTOR signaling (14, 28) and suppresses PTEN loss- induced prostate tumorigenesis (14) and mTOR-dependent renal carcinoma progression (28). We provide evidence from preclinical models and in patients that PML suppresses Akt/mTOR signaling and proliferation (Fig. 1). However, PML is also commonly overexpressed in cancer, including in GBM (12, 29), and has been shown to promote a range of activities that may enhance the growth and progression of cancer, including oncogene-induced senescence (29), hematopoetic stem cell maintenance, and breast cancer tumor cell survival through a peroxisome
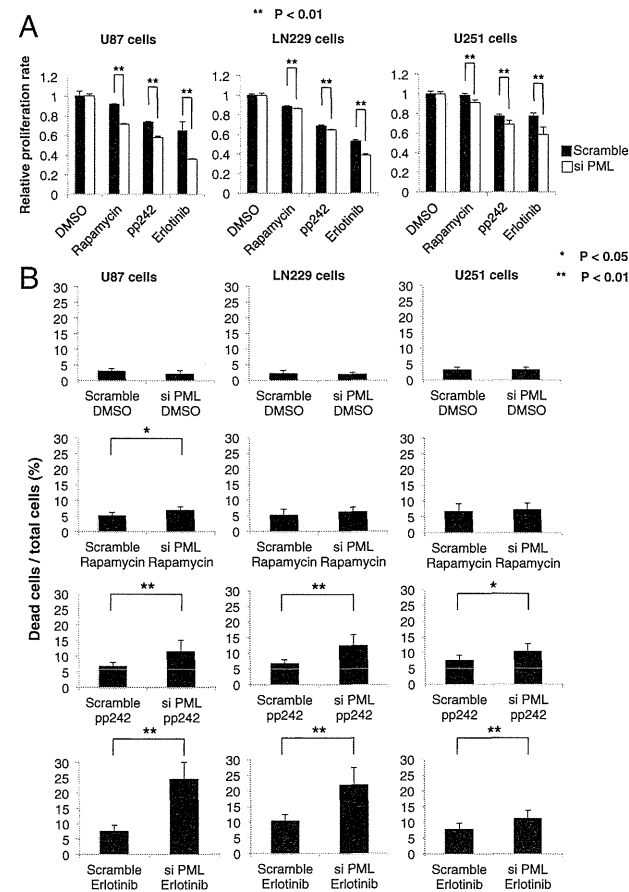

Fig. 4. PML knockdown sensitizes GBM cell lines to EGFR and mTOR targeted therapies. (A) Cell viability assays demonstrate a synergistic effect of PML knockdown and each indicated inhibitor. P values were determined by Student's t test. (B) Effect of PML knockdown and each indicated inhibitor on multiple GBM cell lines analyzed by Trypan blue exclusion. P values were determined by Student's t test.
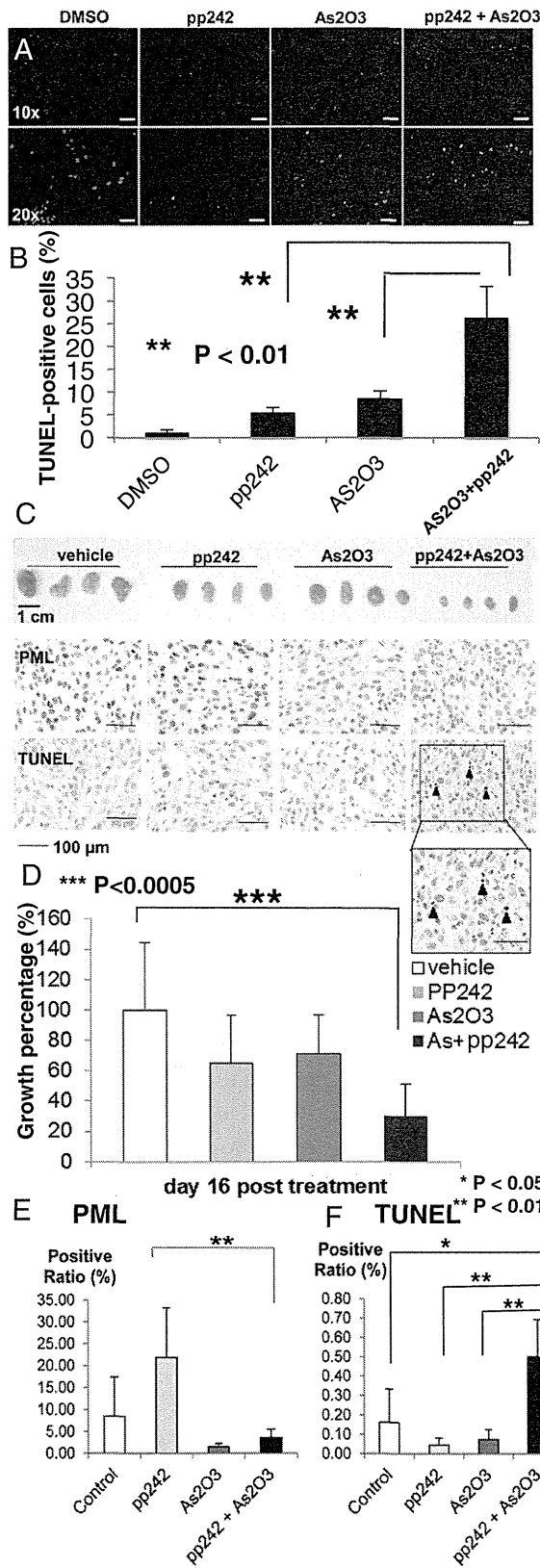
Iwanami et al.

proliferator-activated receptor (PPAR)-γ/fatty acid oxidation-dependent pathway (30, 31). Further, PML has been shown to mediate resistance of leukemias to chemotherapy by supporting maintenance of a "quiescent" tumor cell population (13). Its impact on cancer drug resistance, including drugs that target mTOR or its upstream effectors, in solid tumors including GBM is less clear. Through integration of preclinical studies with analysis of tumor tissue from patients in phase I clinical trials, we demonstrate an important role for PML in mediating mTOR and EGFR inhibitor resistance in GBM. These results present evidence that mTOR inhibition promotes PML up-regulation in patients and that this up-regulation of PML mediates drug resistance.

It is tempting to speculate that PML promotes this resistance by inducing a "quiescent state" through inhibition of Akt/mTOR signaling. However, we cannot formally exclude the possibility that PML may drive resistance through its metabolic prosurvival effects. In fact, this possibility is consistent with our previous observation that EGFR mutant GBMs have enhanced reliance on fatty acid synthesis for survival (17), creating enhanced dependence on fatty acid oxidation for survival (32). Futures studies will be needed to determine the mechanisms by which PML promotes drug resistance in GBM.

mTOR has emerged as a critical target in GBM because it is persistently hyperactivated downstream of the most common GBM alterations including EGFR amplification, EGFR variant III (EGFRvIII) mutation, platelet-derived growth factor receptor (PDGFRα) and hepatocyte growth factor receptor (c-MET) amplification, and PTEN loss (3). We have demonstrated that mTOR inhibition is required for the efficacy of EGFR-targeted therapies (33), suggesting a mechanistic basis by which EGFR tyrosine kinase inhibitors (TKIs) may also potently up-regulate PML expression to promote drug resistance. For both EGFR TKIs and mTOR kinase inhibitors, the potential for converting a cytostatic response, which often yields minimal benefit, to a cytotoxic response by pharmacologically abrogating PML, could potentially represent a significant clinical advance. Our demonstration of a synergism between the two classes of compound in cell death induction underscores this possibility.

Pharmacologically targeting PML represents one of the most exciting success stories for the principle of molecularly guided therapies (10, 11). As_2O_3 targets PML for degradation through a SUMOylation-dependent process (34), potently promoting long-term remission in patients and mice with acute promyelocytic leukemia bearing the PML/RAR fusion (24). Its role in solid cancers has yet to be established. However, As_2O_3 given with standard chemotherapy can be tolerated by GBM patients, as demonstrated in recent clinical trials (35). The results presented here suggest a clinically actionable strategy to combine resistance by combining As_2O_3 with mTOR kinase and EGFR TKIs for the treatment of GBM patients.

Materials and Methods

Nuclei are stained blue. (*B*) Quantification of TUNEL staining. *P* values were determined by Student's *t* test. (*C*) Representative photographs of U87 GBM xenografts treated daily with vehicle, pp242 (60 mg/kg per day by oral gavage), As_2O_3 (2.5 mg/kg intraperitoneally), or combination (*n* = 8 mice per condition). Images of representative PML and TUNEL stains. (*D*) Quantification demonstrating greater than threefold reduction in tumor size for mice treated with combined pp242 and As_2O_3 (*P* < 0.005). (*E* and *F*) Quantification of PML and TUNEL xenograft tumor staining from each treatment conditions.

Fig. 5. As_2O_3 reduces PML and sensitizes GBM cells to mTOR-targeted therapies. (*A*) Representative images demonstrating TUNEL staining (green) to assess apoptotic effect of pp242 and As_2O_3 (2 μM) on U87 cells in vitro.
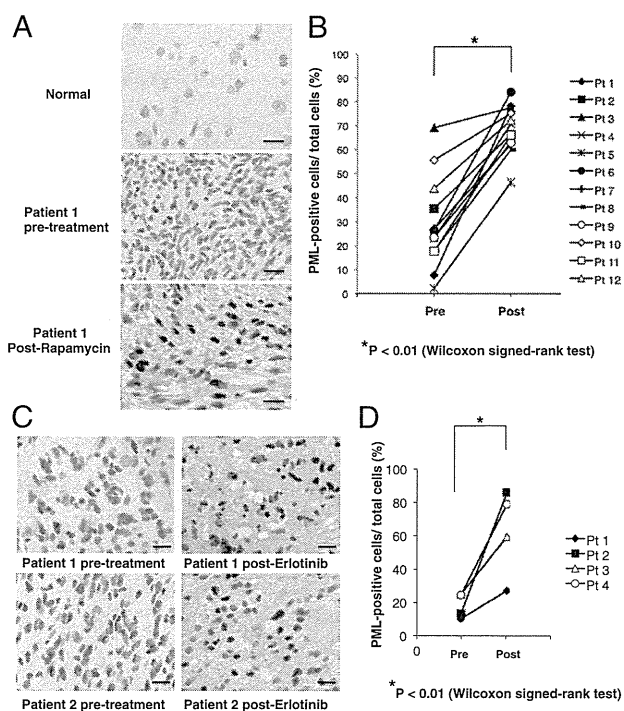
− 52 −

Fig. 6. Rapamycin and erlotinib treatment induces PML expression in GBM patient tumor tissues. (A) Immunohistochemical staining (reddish brown) of PML before and after treatment with rapamycin. Nuclei were counterstained with hematoxylin (blue). (B) Quantification of immunohistochemical staining from >1,000 cells from at least three representative areas of each tumor before and after rapamycin treatment. P value was determined by Wilcoxon signed-rank test. (C) Immunohistochemical staining (reddish brown) of PML before and after treatment with erlotinib. Nuclei were counterstained with hematoxylin (blue). (D) Quantification of immunohistochemical staining from >1,000 cells from at least three representative areas of each tumor before and after erlotinib treatment. P value was determined by Wilcoxon signed-rank test. (Scale bars: 50 μm.) (Magnification: 20x.)

Antibodies and Reagents. We used antibodies directed against the following: phosopho-Akt Ser473, Akt, phospho-S6 Ser235/236, S6, phospho-Erk, Erk, CyclinD1, cleaved PARP (Cell Signaling); β-actin, p21 (Sigma); phospho-EGFR Tyr1086 (Invitrogen); EGFR (Millipore); PML (for Western blotting, Abcam; for immunohistochemisry, Santa Cruz). Reagents used are rapamycin, As_2O_3, polybrene (Sigma), erlotinib (ChemieTex), pp242 (Chemdea). Full details of immunoblot analysis are provided in *SI Materials and Methods*. Stock solutions of inhibitor for rapamycin were made by dissolving in ethanol, erlotinib, and pp242 were made by dissolving in DMSO (Sigma) and stored at −20 °C. Inhibitors were added to each well at final concentrations of 10 nM, 10 μM, and 2 μM, respectively. An equal concentration of ethanol or DMSO served as control. As_2O_3 was diluted by PBS and 10 M NaOH, then pH was adjusted at 8.0 by 12 M HCl.

Plasmid, Retroviral Infection, and siRNA Transfection. Plasmid 22(pLNCX) encoding hemagglutinin (HA) tag-expression construct was obtained from the I.K. laboratory (37). Full details are available in *SI Materials and Methods*. Transfection of siRNA into GBM cell lines was carried out by using Lipofectamine RNAiMAX (Invitrogen) in full serum, with medium

change after 24 h. On-TARGET plus SMARTpool siRNAs (Dharmacon) specifically targeting PML (catalog no. L-006547-000005) and nontargeting control pools of siRNAs (catalog no. D-0018-10-10-05) were used at 10 nM, and cells were harvested 48 h after transfection.

Cell Proliferation and Death Assays. Relative proliferation to control cells with vehicle treatment was checked with a WST-1 Cell Proliferation Assay Kit (Millipore). Cell death was assessed by Trypan blue exclusion (Invitrogen). Full details are given in *SI Materials and Methods*.

Cell Cycle Analyses. Cells were fixed in 70% ethanol diluted in PBS, and the samples were stored at −20 °C. The fixed cells were resuspended in PBS containing 20 μg/mL propidium iodide (Sigma) and 10 μg/mL RNase A (Sigma), and incubated for 10 min at 37 °C. Flow cytometric analysis was performed by using FACSCalibur flow cytometer (Becton Dickinson).

TUNEL Staining and Immunofluorescence Analysis. For TUNEL staining, cells were placed in eight-well chamber slides, incubated with TUNEL Reaction Mixture (Roche) at 37 °C for1 h in the dark, and visualized with a fluorescene microscope (Olympus BX-61). Ten separate, randomly chosen fields on each chamber were imaged, and the numbers of TUNEL-positive cells and whole nuclei were counted. For immunofluorescence analysis with indicated antibodies, cells were fixed with 4% paraformaldehyde in PBS for 10 min, washed twice in PBS, incubated with primary antibodies in PBS containing 3% BSA at 4 °C overnight, and detected with appropriate fluorescence-conjugated secondary antibodies. Full details are presented in *SI Materials and Methods*.

In Vivo Studies. We suspend 1.25×10^6 U87 GBM cells in 100 μL of Matrigel, PBS 1:2 solution, and injected them subcutaneously into the right flank of each 4- to 5-wk-old athymic nude mice. Tumors were measured with an electronic caliper, and volumes were calculated by using width (a), length (b), and depth (c) measurements ($V = a \times b \times c$). Ten days after injection, mice were treated daily with vehicle, 60 mg/kg pp242 by gavage, 2.5 mg/kg intraperitoneally injected As_2O_3 or their combination, respectively. Mice were euthanized when tumor volume of treated mice reached statistical significance compared with control groups. Mice were euthanized in accordance with the University of California at San Diego Institutional Guidelines for Animal Welfare and Experimental Conduct.

Immunohistochemical Assays, Tissue Microarrays, and Image Analysis-Based Scoring. Immunohistochemical staining and analysis of two GBM TMAs was performed, as described (6, 26). Among 140 cases, 87 GBM patient tissue cores were available for analysis based on sufficient high quality tissue. Staining intensity was scored independently by two pathologists who were unaware of the findings of the molecular analyses. See *SI Materials and Methods* for full details.

Statistical Analysis. Results are shown as mean ± SEM. χ^2 for independence test was used to assess correlations between various molecular markers on TMAs. For nonparametric clinical trial data, Wilcoxon rank test was used. Other comparisons in cell proliferation assays, cell death assays, and TUNEL staining were performed with Student's t test, as by analysis of variance, appropriate. $P < 0.05$ was considered as statistically significant.

1. Furnari FB, et al. (2007) Malignant astrocytic glioma: Genetics, biology, and paths to treatment. *Genes Dev* 21(21):2683–2710.
2. Wen PY, Kesari S (2008) Malignant gliomas in adults. *N Engl J Med* 359(5):492–507.
3. Anonymous; Cancer Genome Atlas Research Network (2008) Comprehensive genomic characterization defines human glioblastoma genes and core pathways. *Nature* 455(7216):1061–1068.
4. Parsons DW, et al. (2008) An integrated genomic analysis of human glioblastoma multiforme. *Science* 321(5897):1807–1812.
5. Yecies JL, Manning BD (2011) Transcriptional control of cellular metabolism by mTOR signaling. *Cancer Res* 71(8):2815–2820.

6. Cloughesy TF, et al. (2008) Antitumor activity of rapamycin in a Phase I trial for patients with recurrent PTEN-deficient glioblastoma. *PLoS Med* 5(1):e8.
7. Tanaka K, et al. (2011) Oncogenic EGFR signaling activates an mTORC2-NF-κB pathway that promotes chemotherapy resistance. *Cancer Discov* 1(6):524–538.
8. Bernardi R, Pandolfi PP (2003) Role of PML and the PML-nuclear body in the control of programmed cell death. *Oncogene* 22(56):9048–9057.
9. Bernardi R, Pandolfi PP (2007) Structure, dynamics and functions of promyelocytic leukaemia nuclear bodies. *Nat Rev Mol Cell Biol* 8(12):1006–1016.
10. Andre C, et al. (1996) The PML and PML/RARalpha domains: From autoimmunity to molecular oncology and from retinoic acid to arsenic. *Exp Cell Res* 229(2):253–260.

Iwanami et al.

11. Chen GQ, et al. (1996) In vitro studies on cellular and molecular mechanisms of arsenic trioxide (As2O3) in the treatment of acute promyelocytic leukemia: As2O3 induces NB4 cell apoptosis with downregulation of Bcl-2 expression and modulation of PML-RAR alpha/PML proteins. *Blood* 88(3):1052–1061.

12. Gurrieri C, et al. (2004) Loss of the tumor suppressor PML in human cancers of multiple histologic origins. *J Natl Cancer Inst* 96(4):269–279.

13. Ito K, et al. (2008) PML targeting eradicates quiescent leukaemia-initiating cells. *Nature* 453(7198):1072–1078.

14. Trotman LC, et al. (2006) Identification of a tumour suppressor network opposing nuclear Akt function. *Nature* 441(7092):523–527.

15. Bernardi R, et al. (2004) PML regulates p53 stability by sequestering Mdm2 to the nucleolus. *Nat Cell Biol* 6(7):665–672.

16. Vallian S, et al. (1997) Transcriptional repression by the promyelocytic leukemia protein, PML. *Exp Cell Res* 237(2):371–382.

17. Guo D, et al. (2009) EGFR signaling through an Akt-SREBP-1-dependent, rapamycin-resistant pathway sensitizes glioblastomas to antilipogenic therapy. *Sci Signal* 2(101):ra82.

18. Lu KV, et al. (2009) Fyn and SRC are effectors of oncogenic epidermal growth factor receptor signaling in glioblastoma patients. *Cancer Res* 69(17):6889–6898.

19. Aronson SM (1994) Arsenic and old myths. *R I Med* 77(7):233–234.

20. Mathews V, et al. (2006) Single-agent arsenic trioxide in the treatment of newly diagnosed acute promyelocytic leukemia: Durable remissions with minimal toxicity. *Blood* 107(7):2627–2632.

21. Soignet SL, et al. (1998) Complete remission after treatment of acute promyelocytic leukemia with arsenic trioxide. *N Engl J Med* 339(19):1341–1348.

22. Lallemand-Breitenbach V, et al. (2001) Role of promyelocytic leukemia (PML) sumolation in nuclear body formation, 11S proteasome recruitment, and As2O3-induced PML or PML/retinoic acid receptor alpha degradation. *J Exp Med* 193(12):1361–1371.

23. de Thé H, Chen Z (2010) Acute promyelocytic leukaemia: Novel insights into the mechanisms of cure. *Nat Rev Cancer* 10(11):775–783.

24. Lallemand-Breitenbach V, Zhu J, Chen Z, de Thé H (2012) Curing APL through PML/RARA degradation by As2O3. *Trends Mol Med* 18(1):36–42.

25. Zhao S, Tsuchida T, Kawakami K, Shi C, Kawamoto K (2002) Effect of As2O3 on cell cycle progression and cyclins D1 and B1 expression in two glioblastoma cell lines differing in p53 status. *Int J Oncol* 21(1):49–55.

26. Mellinghoff IK, et al. (2005) Molecular determinants of the response of glioblastomas to EGFR kinase inhibitors. *N Engl J Med* 353(19):2012–2024.

27. Gambacorta M, et al. (1996) Heterogeneous nuclear expression of the promyelocytic leukemia (PML) protein in normal and neoplastic human tissues. *Am J Pathol* 149(6):2023–2035.

28. Bernardi R, et al. (2011) Pml represses tumour progression through inhibition of mTOR. *EMBO Mol Med* 3(5):249–257.

29. Scaglioni PP, et al. (2012) Translation-dependent mechanisms lead to PML upregulation and mediate oncogenic K-RAS-induced cellular senescence. *EMBO Mol Med* 4(7):594–602.

30. Ito K, et al. (2012) A PML–PPAR-δ pathway for fatty acid oxidation regulates hematopoietic stem cell maintenance. *Nat Med* 18(9):1350–1358.

31. Carracedo A, et al. (2012) A metabolic prosurvival role for PML in breast cancer. *J Clin Invest* 122(9):3088–3100.

32. Cvrljevic AN, et al. (2011) Activation of Src induces mitochondrial localisation of de2-7EGFR (EGFRvIII) in glioma cells: Implications for glucose metabolism. *J Cell Sci* 124(Pt 17):2938–2950.

33. Wang MY, et al. (2006) Mammalian target of rapamycin inhibition promotes response to epidermal growth factor receptor kinase inhibitors in PTEN-deficient and PTEN-intact glioblastoma cells. *Cancer Res* 66(16):7864–7869.

34. Zhang XW, et al. (2010) Arsenic trioxide controls the fate of the PML-RARalpha oncoprotein by directly binding PML. *Science* 328(5975):240–243.

35. Grimm SA, et al. (2012) Phase I study of arsenic trioxide and temozolomide in combination with radiation therapy in patients with malignant gliomas. *J Neurooncol* 110(2):237–243.

36. Geschwind DH, et al. (2001) A genetic analysis of neural progenitor differentiation. *Neuron* 29(2):325–339.

37. Nguyen LA, et al. (2005) Physical and functional link of the leukemia-associated factors AML1 and PML. *Blood* 105(1):292–300.

— 54 —

LETTER

Sema3A regulates bone-mass accrual through sensory innervations

Toru Fukuda[1]*, Shu Takeda[1]*, Ren Xu[2,3]*, Hiroki Ochi[1], Satoko Sunamura[1], Tsuyoshi Sato[4], Shinsuke Shibata[5], Yutaka Yoshida[6], Zirong Gu[6], Ayako Kimura[2,7], Chengshan Ma[2,3], Cheng Xu[2,3], Waka Bando[8], Koji Fujita[2,3], Kenichi Shinomiya[2], Takashi Hirai[2], Yoshinori Asou[2], Mitsuhiro Enomoto[2], Hideyuki Okano[5], Atsushi Okawa[2,3] & Hiroshi Itoh[8]

Semaphorin 3A (Sema3A) is a diffusible axonal chemorepellent that has an important role in axon guidance[1-5]. Previous studies have demonstrated that $Sema3a^{-/-}$ mice have multiple developmental defects due to abnormal neuronal innervations[6,7]. Here we show in mice that Sema3A is abundantly expressed in bone, and cell-based assays showed that Sema3A affected osteoblast differentiation in a cell-autonomous fashion. Accordingly, $Sema3a^{-/-}$ mice had a low bone mass due to decreased bone formation. However, osteoblast-specific Sema3A-deficient mice ($Sema3a_{col1}^{-/-}$ and $Sema3a_{osx}^{-/-}$ mice) had normal bone mass, even though the expression of Sema3A in bone was substantially decreased. In contrast, mice lacking Sema3A in neurons ($Sema3a_{synapsin}^{-/-}$ and $Sema3a_{nestin}^{-/-}$ mice) had low bone mass, similar to $Sema3a^{-/-}$ mice, indicating that neuron-derived Sema3A is responsible for the observed bone abnormalities independent of the local effect of Sema3A in bone. Indeed, the number of sensory innervations of trabecular bone was significantly decreased in $Sema3a_{synapsin}^{-/-}$ mice, whereas sympathetic innervations of trabecular bone were unchanged. Moreover, ablating sensory nerves decreased bone mass in wild-type mice, whereas it did not reduce the low bone mass in $Sema3a_{nestin}^{-/-}$ mice further, supporting the essential role of the sensory nervous system in normal bone homeostasis. Finally, neuronal abnormalities in $Sema3a^{-/-}$ mice, such as olfactory development, were identified in $Sema3a_{synasin}^{-/-}$ mice, demonstrating that neuron-derived Sema3A contributes to the abnormal neural development seen in $Sema3a^{-/-}$ mice, and indicating that Sema3A produced in neurons regulates neural development in an autocrine manner. This study demonstrates that Sema3A regulates bone remodelling indirectly by modulating sensory nerve development, but not directly by acting on osteoblasts.

Sema3A, the first member to be identified from the large semaphorin family, is a well-known chemorepellent[1,2,5]. Sema3A, which is secreted from target tissue, forms steep gradients and causes inhibition of axonal outgrowth and cell migration in a concentration-dependent manner[4,5]. This repulsive signal is essential for neural development[3]. Indeed, $Sema3a^{-/-}$ mice have several neuronal defects, including abnormalities in the cerebral cortex, olfactory system and axon projections of dorsal root ganglia (DRG) neurons[6-8]. More recently, Sema3A has been implicated in additional physiological functions, such as immunoregulation, angiogenesis and cancer development[5,9-12]. Osteoblasts and osteoclasts express semaphorin family proteins, and recent reports suggested that these proteins regulate bone remodelling locally by acting as paracrine signalling molecules[13-15]. To address the role of Sema3A in bone remodelling, we first analysed the expression in bone of: $Sema3a$; $Nrp1$, encoding a Sema3A receptor; and $Plxna1, 2, 3$ and 4, encoding Sema3A co-receptors[1]. $Sema3a$ was ubiquitously expressed in many tissues including bone (Fig. 1a), indicating its diverse physiological action. The expression of $Sema3a$ increased during osteoblast differentiation (Fig. 1b) and decreased during osteoclast differentiation (Fig. 1c). Plxna1, 2 and 3 and Nrp1 were expressed in osteoblasts (Fig. 1d and Supplementary Fig. 1), indicating that Sema3A may have a role in osteoblast differentiation. Therefore, we analysed $Sema3a^{-/-}$ mice. $Sema3a^{-/-}$ mice showed a 25% decrease in bone mass due to a decrease in bone formation without an overt change in bone resorption at 3, 6 and 12 months of age, although a non-significant increase was observed in a serum bone resorption marker (Fig. 1e–g and Supplementary Figs 2b, 3), demonstrating that Sema3A accelerates bone formation. To determine whether the defect in bone formation in $Sema3a^{-/-}$ mice was cell autonomous, we isolated osteoblasts from wild-type and $Sema3a^{-/-}$ mice. In accordance with in vivo observations, $Sema3a^{-/-}$ osteoblasts showed a defect in differentiation, as observed
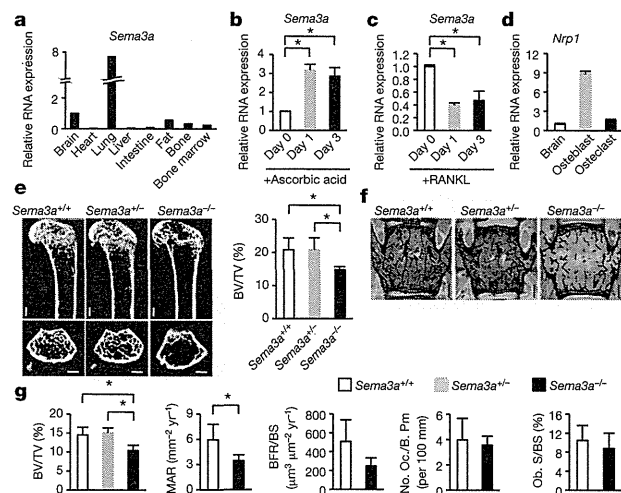

Figure 1 | $Sema3a^{-/-}$ mice have low bone mass. a–d, Gene expression analysis of $Sema3a$ (a–c) and its receptor (d) ($n = 4$). e–g, Analysis of $Sema3a^{-/-}$ mice. Microcomputed tomography (micro-CT) analysis (e), histological analysis (f, g) in 3-month-old mice (male, $n = 8$ for $Sema3a^{+/+}$, $n = 6$ for $Sema3a^{+/-}$, $n = 10$ for $Sema3a^{-/-}$). Bone volume/tissue volume (BV/TV; %), mineral apposition rate (MAR; mm yr^{-1}), bone formation rate/bone surface (BFR/BS; mm^3 mm^{-2} yr^{-1}), osteoclast number/bone perimeter (No. Oc./B. Pm) and osteoblast surface/bone surface (Ob. S/BS; %). Note a decrease of bone mass in $Sema3a^{-/-}$ mice. Scale bars, 500 μm. Error bars, mean ± standard deviation (s.d.). *$P < 0.05$.

[1]Department of Internal Medicine, School of Medicine, Keio University, Shinanomachi 35, Shinjyuku-ku, Tokyo 160-8582, Japan. [2]Department of Orthopedic Surgery, Tokyo Medical and Dental University, Yushima 1-5-45, Bunkyo-ku, Tokyo 113-8549, Japan. [3]Global Center of Excellence (GCOE) Program, International Research Center for Molecular Science in Tooth and Bone Diseases, Yushima 1-5-45, Bunkyo-ku, Tokyo 113-8549, Japan. [4]Department of Oral and Maxillofacial Surgery, Saitama Medical University, Morohongo 38, Moroyama-machi, Iruma-gun, Saitama 350-0495, Japan. [5]Department of Physiology, School of Medicine, Keio University, Shinanomachi 35, Shinjyuku-ku, Tokyo 160-8582, Japan. [6]Division of Developmental Biology, Cincinnati Children's Hospital Medical Center, Cincinnati, Ohio 45229, USA. [7]Hard Tissue Genome Research Center, Tokyo Medical and Dental University, Yushima 1-5-45, Bunkyo-ku, Tokyo 113-8549, Japan. [8]Section of Nephrology, Endocrinology and Metabolism, Department of Internal Medicine, School of Medicine, Keio University, Shinanomachi 35, Shinjyuku-ku, Tokyo 160-8582, Japan.
*These authors equally contributed to this work.

by a decrease in alkaline phosphatase activity and the expression of osteoblast markers (Supplementary Fig. 2c). We next determined whether treatment with Sema3A affected osteoblast and osteoclast differentiation and proliferation. Sema3A accelerated osteoblastic differentiation when added exogenously in culture media (Supplementary Fig. 2d). The knockdown of *Sema3a* in osteoblasts hampered their differentiation, and treatment with Sema3A rescued the defects in osteoblast differentiation in *Sema3a* knocked-down osteoblasts (Supplementary Fig. 2e). The expression of a dominant-negative form of Rac1 inhibited Sema3A-dependent osteoblast differentiation (Supplementary Fig. 2f), which indicates that Sema3A regulates osteoblast differentiation through the activation of Rac1, a signalling molecule required for the action of Sema3A on the collapse of the growth cone[16]. Sema3A treatment did not affect osteoblast proliferation (Supplementary Fig. 4). By contrast, the treatment of osteoclast precursors with Sema3A caused a decrease in osteoclast differentiation, as shown by a decrease in the number of multinucleated TRAP-positive osteoclasts and the expression of osteoclast marker genes, such as cathepsin K (Supplementary Fig. 2g). These results suggested that Sema3A functions in an autocrine fashion to stimulate osteoblast differentiation and inhibit osteoclast differentiation, thereby increasing bone mass.

To determine whether Sema3A affected bone metabolism in an autocrine manner *in vivo*, we generated osteoblast-specific Sema3A-deficient mice using α1(I)-Cre mice (*Sema3a$_{col1}$*$^{-/-}$ mice)[17]. *Sema3a$_{col1}$*$^{-/-}$ mice developed normally without any gross abnormality. The expression of *Sema3a* in the bones of *Sema3$_{col1}$*$^{-/-}$ mice was decreased (Supplementary Fig. 5a), and the osteoblasts isolated from *Sema3a$_{col1}$*$^{-/-}$ mice showed a defect in osteoblast differentiation *in vitro* (Supplementary Fig. 5b, c), as observed for *Sema3a*$^{-/-}$ osteoblasts isolated from *Sema3a*$^{-/-}$ mice (Supplementary Fig. 2c). However, *Sema3a$_{col1}$*$^{-/-}$ mice had normal bone formation and bone mass (Fig. 2a–c and Supplementary Fig. 5d). Moreover, another osteoblast-specific knockout mouse created using the osx-Cre mouse[18], which deletes Sema3A in early osteoprogenitors, did not develop any bone abnormalities (*Sema3a$_{osx}$*$^{-/-}$ mice) (Supplementary Fig. 5e). Taken together, these results indicate that the lack of Sema3A in osteoblasts is not the sole cause of bone abnormalities in *Sema3a*$^{-/-}$ mice.

Bone remodelling has been shown to be regulated by the central and peripheral nervous systems[19]. Thus, we examined the necessity of neuron-derived Sema3A in the maintenance of normal bone mass by deleting Sema3A in neurons using synapsin-I-Cre mice[20] or nestin-Cre mice[21] (*Sema3a$_{synapsin}$*$^{-/-}$ and *Sema3a$_{nestin}$*$^{-/-}$ mice, respectively). *Sema3a$_{synapsin}$*$^{-/-}$ and *Sema3a$_{nestin}$*$^{-/-}$ mice developed normally without any growth retardation or perinatal lethality, which were observed in *Sema3a*$^{-/-}$
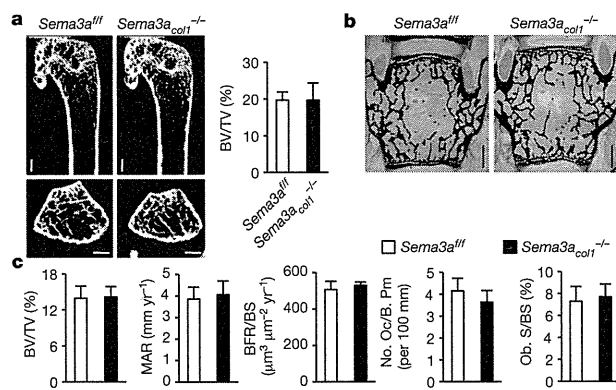
mice[6]. Surprisingly, *Sema3a$_{synapsin}$*$^{-/-}$ and *Sema3a$_{nestin}$*$^{-/-}$ mice showed significant reductions in bone mass in both males and females, in both vertebrae and long bones, and in both trabecular and cortical bones; that is, in all of the bones in the entire body at any stages analysed (Fig. 3b–d and Supplementary Figs 6, 7b–d, f–h). This low bone mass phenotype was accompanied by decreased bone formation and osteoblast differentiation *in vivo* (Fig. 3d, e). *Sema3a$_{synapsin}$*$^{-/-}$ primary osteoblasts did not show overt abnormalities in osteoblast differentiation *in vitro* (Supplementary Fig. 8a, b), whereas *Sema3a$_{nestin}$*$^{-/-}$ primary osteoblasts exhibited a defect (Supplementary Fig. 8c, d), indicating a decreased differentiation state of the osteoblast precursors, some of which are known to be nestin positive[22]. Interestingly, expression of *Sema3a* in the bones of *Sema3a$_{synapsin}$*$^{-/-}$ mice was decreased (Fig. 3a), suggesting that neurons in the bones are responsible for a substantial amount of Sema3A expression. *Sema3a$_{synapsin}$*$^{-/-}$ and *Sema3a$_{nestin}$*$^{-/-}$ mice showed a decrease in bone mass (Fig. 3b–d and Supplementary Figs 6a, b, 7b–d, f–h) whereas *Sema3a$_{col1}$*$^{-/-}$ mice had normal bone mass (Fig. 2a–c and Supplementary Fig. 5d) in the presence of comparable decreases in the expression of *Sema3a* in bones in *Sema3a$_{col1}$*$^{-/-}$, *Sema3a$_{synapsin}$*$^{-/-}$ and *Sema3a$_{nestin}$*$^{-/-}$ mice (Fig. 3a and Supplementary Figs 5a, 7a). This indicated that the decreased expression of *Sema3a* in bone was not the cause of the bone abnormality. In line with this observation, *Sema3a*$^{+/-}$ mice, in which the expression of *Sema3a* in bone was decreased to a similar extent to in *Sema3a$_{col1}$*$^{-/-}$, *Sema3a$_{synapsin}$*$^{-/-}$ and *Sema3A$_{nestin}$*$^{-/-}$ mice (Fig. 3a and Supplementary Figs 2a, 7a), had normal bone mass (Fig. 1e, f).

Because Sema3A is a well-known axon guidance molecule, especially as a chemorepellent, we tested whether the development of the nervous system was affected in *Sema3a$_{synapsin}$*$^{-/-}$ and *Sema3a$_{nestin}$*$^{-/-}$ mice. Surprisingly, nerve innervations were significantly decreased in the bones of both mice, as shown by a decrease in neurofilament-positive fibres (Fig. 4a and Supplementary Figs 9, 10). Dopamine β-hydroxylase (DBH)-positive sympathetic nerve fibres, which inhibit bone mass accrual[19], were not significantly affected (Fig. 4b and Supplementary Fig. 10), and these fibres did not colocalize with neurofilament-positive fibres (Supplementary Fig. 11b). Neurofilament-positive fibres in bone are considered to be calcitonin-gene-related peptide (CGRP)-positive sensory fibres[23], and indeed, CGRP-positive and transient receptor potential cation channel subfamily V member 1 (TRPV1)-positive fibre innervations were decreased in *Sema3a$_{synapsin}$*$^{-/-}$ and
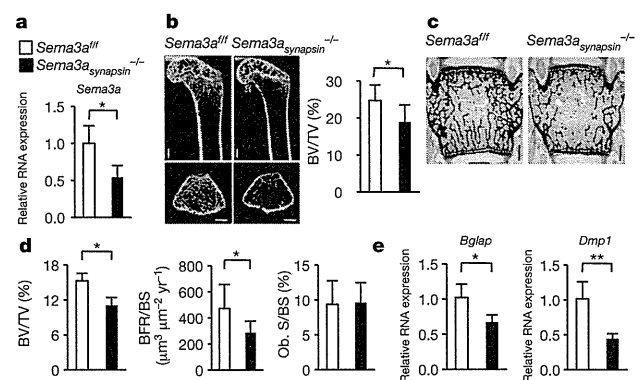
Figure 2 | **Osteoblast-derived Sema3A does not affect bone mass *in vivo*.** a–c, Analysis of osteoblast-specific Sema3A-knockout mice. **a**, Micro-CT analysis of the femurs of 3-month-old *Sema3a$_{col1}$*$^{-/-}$ mice and their littermates (male, $n = 7$). **b, c**, Histological analyses of vertebrae (male, $n = 7$). Note an absence of bone abnormalities in *Sema3a$_{col1}$*$^{-/-}$ mice. Scale bars, 500 μm. Error bars, mean ± s.d.

Figure 3 | **Neuron-derived Sema3A is indispensable for normal bone mass *in vivo*.** a–e, Sema3A was conditionally inactivated in neurons using synapsin-I-Cre mice (*Sema3a$_{synapsin}$*$^{-/-}$ mice) at 3 months. **a**, Quantitative real-time PCR analysis (male, $n = 4$). Note a significant decrease of *Sema3a* expression in *Sema3a$_{synapsin}$*$^{-/-}$ mouse femurs. **b–d**, Micro-CT analysis of femurs (**b**) or histological analyses of vertebrae (**c, d**) from *Sema3a$_{synapsin}$*$^{-/-}$ mice (male, $n = 8$ for *Sema3a$^{f/f}$*, $n = 6$ for *Sema3a$_{synapsin}$*$^{-/-}$). Note a decrease of bone mass in *Sema3a$_{synapsin}$*$^{-/-}$ mice. Scale bars, 500 μm. **e**, Expression of bone marker genes in femurs (male, $n = 4$). Note a decrease in osteoblast differentiation in *Sema3a$_{synapsin}$*$^{-/-}$ mice. Error bars, mean ± s.d. *$P < 0.05$, **$P < 0.01$.

— 56 —